Review Vol. 11, No. 9 / 1 Sep 2021 / Optical Materials Express 3245
Optical Materials EXPRESS

Photonic crystal lasers: from photonic crystal surface emitting lasers (PCSELs) to hybrid external cavity lasers (HECLs) and topological PhC lasers [Invited]

S. Iadanza,[1,2,*] A. A. Liles,[3] S. M. Butler,[1,2] S. P. Hegarty,[1,2] and L. O'Faolain[1,2]

[1]Centre for Advanced Photonics & Process Analysis, Cork Institute of Technology, Rossa Ave Bishopstown, Cork T12P928, Ireland
[2]Photonics, Tyndall National Institute, Lee Maltings Complex Dyke Parade, Cork T12 R5CP, Ireland
[3]INTEC, imec - UGent, Technologiepark Zwijnaarde 126, 9052 Ghent, Belgium
[*]simone.iadanza@mycit.ie

Abstract: Photonic crystals (PhC) represent an important class of silicon photonics components employed as wavelength selective resonators to act as narrow-band mirrors in integrated lasers due to their small footprint, high surface area, and Q-factor/volume ratio that enables efficient confinement of light, required for improved performances of the laser. These properties of PhCs are key for the potential deployment of PhC based high power, energy efficient and versatile semiconductor lasers for telecom, datacom, optical sensing and biomedical applications. In this paper, we report the main advances on PhC based lasers from photonic crystal surface-emitting lasers (PCSELs) to the new hybrid external cavity laser (HECLs) configurations.

1. Introduction

In recent years, we have seen an unprecedented growth of data communication technology that has pervasively influenced the very shape of our society. The power now consumed by Information and Communications Technologies (ICT) far exceeds that generated by solar power worldwide. Society implicitly expects access to an exponentially growing amount of computing power, which is integral to applications ranging from social networking and online gaming to DNA sequencing and planet hunting. The employment of optics in telecom networks, including the widely used active optical cables (AOCs) have mitigated the overall power consumption bringing optical interconnects into datacentres and supercomputers [1–4]. However, the still growing power consumption issue is a direct consequence of the electrical interconnects that processors use to move data, which dissipate a huge portion of the operating power and are limited in speed [5]. In order to limit the power consumption further, there is therefore an urgent need to introduce optical interconnects at much shorter distances: on circuit boards inside each rack, from processor to processor, on CMOS chips [6,7]. To realize such short-distance optical interconnects, compact and energy efficient components able to encode light into digital bits are needed. Moreover, compact and energy efficient semiconductor lasers are also needed for present and emerging fields such as on-chip optical computing, optical sensing and biomedical applications such as bioimaging and optical tomography.

Current semiconductor laser technology has many types of compact and energy efficient devices to offer, depending on the requirements of the application. In the case of optical data transmission, one of the most interesting solutions is based on ultra-low power consumption direct modulation of light. For these types of devices, the most critical parameters to achieve

#430748 https://doi.org/10.1364/OME.430748
Journal © 2021 Received 4 May 2021; revised 7 Jul 2021; accepted 8 Jul 2021; published 1 Sep 2021

Optical Materials EXPRESS

ultra-low power consumption are the effective size of the light emitting region, and the volume of the device requiring modulation. One of the most common examples of directly modulated lasers used in current datacentres are Distributed Feedback (DFB) lasers. They typically contain active regions spanning hundreds of square micrometres, which leads to data generation energy costs in the range of 1 pJ/bit [8–10]. A further decrease in the energy budget for data generation has been achieved by Vertical-Cavity Surface Emitting Lasers (VCSELs), with a reduced active area of a few square micrometres and a cost per bit of around 100 fJ [11,12]. However, this energy cost is still an order of magnitude too high for optical interconnects to address the ICT energy problem [7]. A great research effort has been carried out by various groups to bring the energy cost of directly modulated lasers down to ~10 fJ/bit. One step towards a solution has been made by employing PhCs as part of the laser cavity, which offer low loss confinement of light in volumes of the order of ~λ^3, fine wavelength selectivity and high reflectivity, thus reducing the length of the active region needed for modulation to a couple of microns. Moreover, PhCs are unlocking a variety of new functionalities for semiconductor lasers that were not available before, such as: polarization and beam pattern control, one-dimensional beam steering, and high-power operation with high beam quality in the watt range [13–16]. For all these reasons, PhC based relatively high-power semiconductor lasers with completely controllable beams have been developed, such as Photonic Crystal Surface Emitting Lasers (PCSELs), offering great potential for optical imaging, LIDAR, biometric and datacentres applications. PCSELs are described in the first section of this review. The tight spatial confinement at the nanoscale of PhCs helped reduce the energy cost of directly modulated lasers to 8 fJ/bit, with the development of Lambda-Scale Embedded Active-Region Photonic Crystal (LEAP) lasers, first proposed by Notomi et al. [16]. LEAP lasers will be described in the second section of this paper.

PCSELs and LEAP lasers are based on PhCs directly patterned onto III-V materials. This poses major cost and processing issues regarding their integration on CMOS and Si/Si3N4 photonic integrated circuit (PIC) platforms as required for optical interconnects. Direct growth on silicon of the III-V materials used as gain for these types of lasers is extremely difficult, due to lattice constant mismatches and compatibility challenges [17,18]. These challenges have generated strong interest towards hybrid [19] and heterogeneous [20] laser integration schemes. The former relies on the butt-coupling of commercially available reflective semiconductor optical amplifiers (RSOAs) to wavelength selective reflective components such as Bragg gratings and PhCs to form the laser cavity (here referred to as Hybrid External Cavity Lasers: HECLs). The latter consists in wafer or die bonding of III-V material on silicon before the definition of a laser cavity through III-V and Si patterning and relying on evanescent coupling of the optical mode from the III-V gain to the PIC. On one hand, the potential for relatively low-cost and relaxed bonding misalignment tolerances of heterogeneous integration has stimulated significant research interest – as evidenced by a wide variety of configurations of heterogeneously integrated laser devices demonstrated in literature, such as quantum dot (QD) lasers [21], Fabry-Perot (FP) lasers [22], distributed feedback (DFB) lasers [23] and micro ring resonators (MRRs) [24], microdisks [25], gratings [26] and 1D photonic crystals (PhC) based lasers [27]. Drawbacks of the evanescent gain-silicon photonic circuit coupling of heterogeneously integrated lasers include lower modal gain, and the presence of a bonding layer degrading performance. On the other hand, the higher wall-plug efficiency and possibility to inject light directly into the silicon waveguide offered by hybrid integration schemes provides great design flexibility and a wider parameter space that makes the Hybrid External Cavity laser (HECLs) an attractive solution.

The HECL concept allows independent optimization of the gain and of the passive chip constituting the wavelength selective mirror of the laser cavity, allowing one to externally modulate the laser and to tailor the laser cavity length, wavelength, bandwidth and reflectance of the mirrors. It also allows for higher thermal conductivity and wall-plug efficiencies [28,29] compared to heterogeneous integrated lasers. Although the typical wall-plug efficiencies of

Optical Materials EXPRESS

HECLs in the range 10-13% [29] are still lower than those of monolithic III-V lasers, their laser output is directly injected into the silicon photonic circuits, leading to equivalent power propagating in the optical network. As the total energy cost-per bit in data transmission is recently becoming more and more influenced by the laser power efficiency, HECLs are gaining popularity in a large number of configurations, using Distributed Bragg Reflectors (DBRs) [22,30–33], MRRs [34,35], Sagnac interferometers [36] and 2D PhCs [37–40] as wavelength selective mirrors. These energy-efficient lasers have the potential to be heavily employed not only for data communication, but also in other fields such as optical sensing, biomedical devices, compact diagnostics and high accuracy metrology [24]. Particularly, Photonic Crystals based HECLs, with their high tunability, low footprint and high light confinement characteristics, will be discussed in further detail in the sections later. Furthermore, this review will also briefly discuss recent alternatives for light confinement, in the form of Bound-In-Continuum (BIC) states generated by exploiting symmetric properties in PhCs and PhC based topological lasers. The BIC states confined in the continuum spectrum of extended states of the medium, which allows very high Quality factors (up to infinity in the ideal case) are currently becoming very interesting for potential applications in high power lasing, such as in the case of BIC-based PCSELs ([13,14], [41–43]), sensing [44] and filtering [45], while topological protected lasing regimes [46] could enable the development of alternative laser prototypes with exotic physical properties.

2. Photonic crystal surface emitting lasers (PCSELs)

One of the main advantages of Vertical Cavity Surface Emitting Lasers (VCSELs) is the emission of light normal to the device surface. This geometry allows for the coupling of the laser output directly into optical fibres normal to the wafer surface, offering easily testable arrays of devices on a single wafer, which improves yield and lowers manufacture costs. This advantageous architecture inspired the development of a new family of vertically emitting devices with improved performance (smaller active area, lower power consumption, better integrability and new functionalities) by using PhCs as the laser cavity mirrors, rather of the vertical DBRs typically used in VCSELs. In fact, thanks to the photonic bandgap properties of PhCs, this family of vertically emitting semiconductor lasers, called PCSELs, maintain similar performance as VCSELs technology with reduced footprint. In addition, extra beam shaping functionalities, such as on-chip polarization, beam pattern and directionality control, not possible in the other semiconductor lasers, eliminate the need for bulky external optical elements.

The current versions of PCSELs are based on squared-lattice PhCs, which are better suited for high power single-mode lasing and beam shaping [47] than triangular-lattice PhCs [48,49]. Square lattice PhCs can be optimized to produce near-diffraction-limited circular output beams and other finely tuned beam shapes while maintaining a highly coherent single-mode. Schematics of a PCSEL and a VCSEL are shown in Fig. 1, to highlight the devices differences and similarities. As depicted in Fig. 1(b), a PCSEL typically consists of a Multiple Quantum Well (MQW) gain section (although QDs have also been used [50]), sandwiched between cladding layers, with a Photonic Crystal layer (characterized by the lattice constant a) embedded on top of the active material. Electron blocking layers and metal contacts are also employed for the optoelectronic operation of the device.

The vertical emission of the laser is achieved thanks to the tailored properties of the photonic bandgap arising from the photonic crystal. At a specific singularity point of the photonic bandgap, four fundamental light waves are allowed to propagate in the photonic crystal plane and can transfer energy between each other via higher-order Bloch modes related to the diffraction of the PhC lattice. This results in the generation of four 2D broad-area cavity modes at the band edges of the PhC bandgap, which can strongly or weakly couple to radiative modes outside of the photonic crystals through diffraction, giving rise to the vertically emitted output of the PCSEL. Of the four, two modes characterized by symmetric electric field distributions show high coupling efficiency

Optical Materials EXPRESS

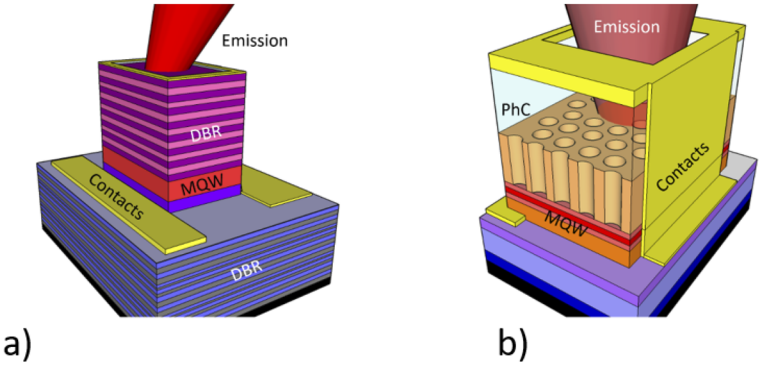

Fig. 1. a) Schematics of a VCSEL, b) Schematics of a PCSEL

with the radiative modes (therefore leaking out of the PhC), and do not contribute to the lasing due to their high threshold gain. Conversely, the anti-symmetric (and rotationally symmetric) field distributions of the other two modes overlap weakly with the radiative counterparts, leading to the confinement of the modes in the laser cavity, which maximizes the interaction with the gain material and establishes the lasing mechanism. The stable single mode lasing regime is reached by tailoring the shape of the holes of the PhC to separate the threshold gains of these two modes. The photonic crystal is fabricated on top of the gain and the overlap of the PhC band edge with the gain emission is obtained by tailoring the lattice constant a, while beam shaping, polarization, and directional control of the PCSEL output is achieved by further design of the air-holes shape and size of the photonic crystal though the study of the related photonic bandgap. The integration of the photonic crystal onto the gain chip is normally achieved by wafer bonding approaches [51], and epitaxial growth techniques [52].

In addition to their high-power output and good beam shape, which makes PCSELs well-suited for LIDAR and imaging applications, their energy efficiency and compact architecture has also directed interest towards their potential employment for direct light modulation applications in telecommunications, leading to the development of Modulated PCSELs (M-PCSELS) [53].

3. Lambda-scale embedded active-region photonic crystal (LEAP) lasers

The great need for a semiconductor light source integrated on Silicon Photonic (SiP) circuits, discussed in the introduction, has stimulated the development of another class of laser devices based on photonic crystal cavities, characterized by a laser output parallel to the plane of the wafer and very small sizes, - desirable qualities for SiP integration and low power consumption, respectively. These edge emitting lasers based on PhC resonators were defined for the first time in 2012 as Lambda-Scale Embedded Active-Region Photonic Crystal (LEAP) lasers by Takeda et al. [54].

LEAP lasers consist of a gain section (typically InGaAsP wavelength-scale MQW buried heterostructures on InP substrates) embedded in an electron-beam lithography patterned PhC cavity. The active region is normally fully contained in the PhC cavity, with sizes of a few μm^2. The PhC cavity confines the light emitted from the small active region forming the laser cavity – shown schematically in Fig. 2. The PhC photonic bandgap is engineered to overlap with the gain spectrum, while the PhC resonances select the lasing wavelengths. Ion implantation of Si and diffusion of Zn are used to form a p-i-n junction lateral to the PhC cavity, connected to metal pads acting as electrical contacts for current injection into the gain section.

Finally, to convert the laser output from normal to the plane of the wafer to an in-plane propagation to enable coupling LEAP lasers with optical filters and photodetectors in planar

Optical Materials EXPRESS

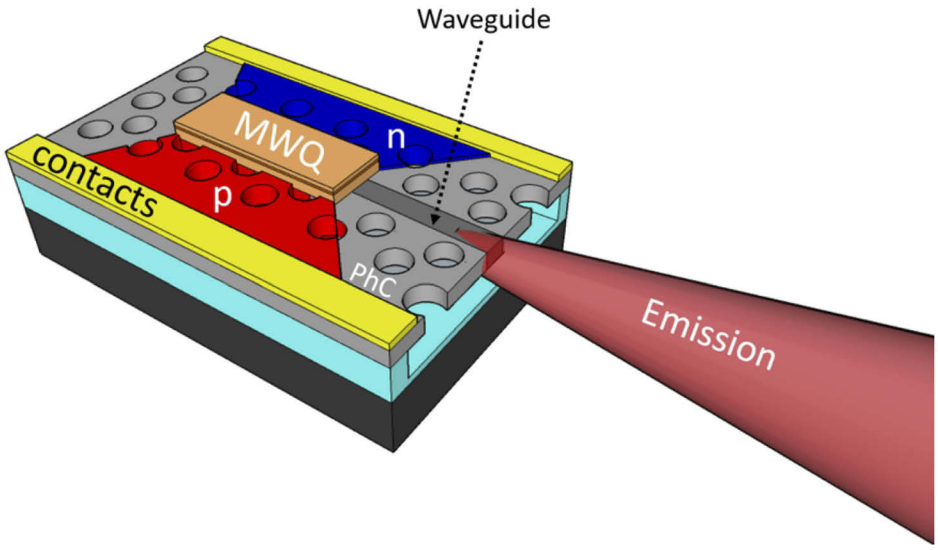

Fig. 2. Schematics of a LEAP laser, in which p and n represent a pn junction fabricated on the PhC cavity.

photonic circuits, various approaches have been used. Two of the most popular are: i) wafer bonding the LEAP laser onto a Si grating coupler attached to a Si wire waveguide [55] and ii) evanescently side-coupling the PhC cavity modes to a photonic crystal waveguide [56,57], subsequently coupled to a Si wire waveguide to inject light in the PIC (Fig. 2).

Direct modulation of the LEAP laser has also been achieved in a number of works [16] and [54,11, 59] showing speeds in the GHz range, with a maximum modulation speed of 20 Gb/s [59], opening the possibility to use these lasers for short-range Telecoms.

In terms of performances of these lasers, apart from the achievement of single-mode lasing [57], the very small active region allows very low lasing threshold, demonstrated by many works [56–58], with [56] showing a record low threshold current of 31 μA for a LEAP laser on Si, [16] reporting the lowest threshold power of 1.5 μW and [54] demonstrating the lowest power consumption reported, namely 4.4 fJ/bit.

4. Hybrid external cavity lasers (HECLs)

All the above-mentioned lasers have been realized entirely on III-V platforms, while, in order to take advantage of the high volume and low-cost manufacture of microelectronics industry, the development of these components needs to be directed more and more towards the silicon platform. Silicon offers a series of advantages over III-V materials in terms of lower optical absorption loss and thermal properties, yet the inefficient optical emission of silicon renders III-V gain media necessary for laser applications.

This led to the development of an alternative approach for the formation of hybrid lasers for SiP PICs, consisting in the combination of III-V Reflective Semiconductor Optical Amplifiers (rSOAs) with external wavelength selective reflectors on the SiP chip. This approach has lately gained considerable popularity, as it allows for the independent design, fabrication, and optimization of the two parts, in a cost-effective way. At the same time, it relies on mature integration/assembly technologies (e.g., flip-chip bonding) that can support the low to medium manufacturing volumes required by the integrated photonics market into the near future.

Hybrid External Cavity lasers (HECLs) consist of a reflective gain chip, typically a reflective Semiconductor Optical Amplifier (rSOA) die, coupled (typically butt-coupled/edge-coupled)

Optical Materials EXPRESS

to a waveguide of a silicon photonic circuit containing a wavelength selective reflective device (e.g., Bragg Gratings, Photonic Crystal cavities – discussed more in detail in the next section). These two components form the laser cavity, delimited by the high-reflection (HR) coated facet of the rSOA on one side and the reflective component on the silicon platform on the other side, as shown in the schematics in Fig. 3.

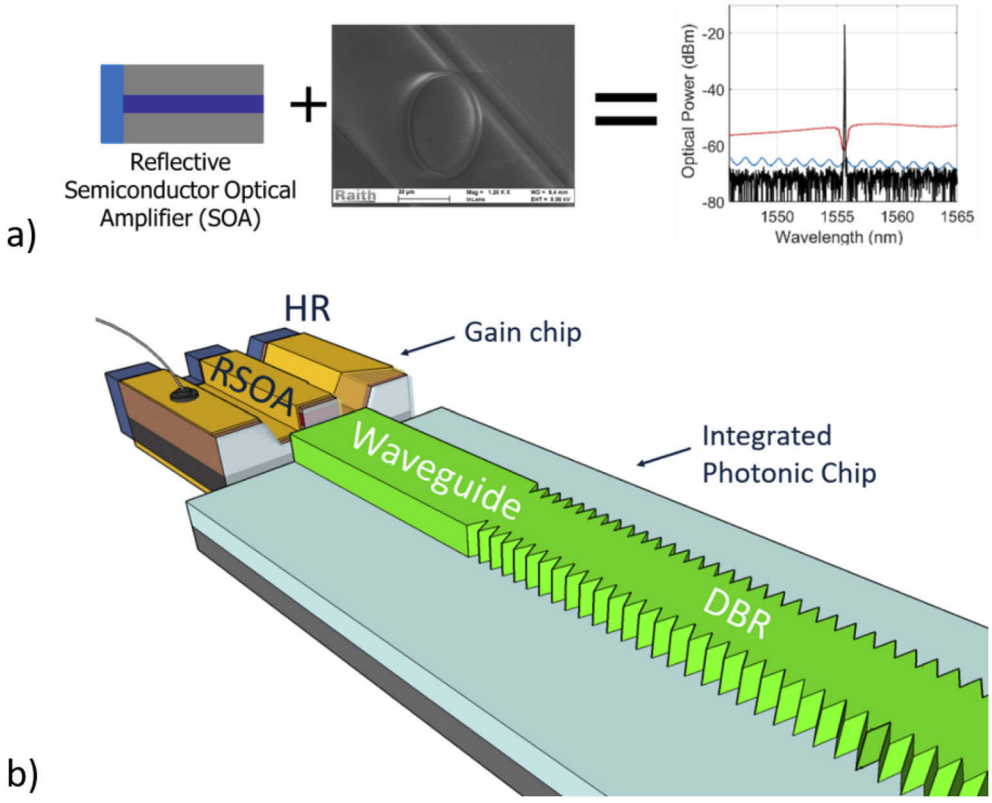

Fig. 3. a) Schematic representation of a HECL composed by an rSOA coupled to a Silicon MRR, b) 3D schematics of a HECL comprising a rSOA edge-coupled to a DBR on Silicon Nitride (SiN)

For the operation of the laser, charge carriers are injected in the rSOA, which then recombine in the quantum wells of the active region generating photons. The emitted light is then coupled to the waveguide of the silicon photonic circuit and propagates towards the reflector in its path. The light component that is not selected by the narrowband mirror is transmitted to the output of the waveguide, while the selected component is partially reflected back to the rSOA, stimulating the recombination: an amplification loop is therefore generated. The lasing wavelength emitted by the laser cavity corresponds to the longitudinal laser cavity mode that overlaps with the reflection band of the selective mirror. The defining parameters of the HECL can be derived from the overlapping of the resonance characteristics of the laser cavity and the gain spectrum. This is similar to the case of DBR laser, with the difference that in HECLs the cavity is a composite between the gain and the passive chip, leading to a longitudinal mode spacing $\Delta\lambda$ that depends on the total optical path resulting from the sum of the optical lengths of the different materials. This relation is condensed in **Eq. (1)**:

$$\Delta\lambda = \frac{\lambda^2}{2(L_{gain}n_{gain} + L_{wg}n_{wg} + L_r n_r)}. \tag{1}$$

Optical Materials EXPRESS

Where λ is the wavelength of the laser, L_{gain} and n_{gain} are the length and refractive index of the gain chip respectively, L_{wg} and n_{wg} the length and refractive index of the waveguide and L_r and n_r the length and refractive index of the reflector respectively. The quantity $L_{gain}n_{gain}$ represents the optical path of light in the gain chip while $L_{wg}n_{wg} + L_rn_r$ is the fraction of the total optical path corresponding to the passive material. The lasing condition is met when the optical gain is balanced out by the round-trip losses experienced by light in the cavity, so that the lasing threshold g in steady-state operation can be defined as:

$$g = \alpha_i + \left(\frac{1}{L_{gain}}\right) \ln\left(\frac{1}{k^2(r_{gain}r_r)}\right) \tag{2}$$

where α_i is the optical loss coefficient, r_{gain} and r_r are the reflectivities of the HR coated facet of the gain chip and the photonic circuit resonator respectively. The definition of the lasing threshold in **Eq. (2)** is similar to the one for DFB lasers, with the difference of an added k^2 term representing the coupling coefficient between the gain and the passive chip.

This type of device is compatible with chip bonding integration approaches [60], enabling high yield and better performances due to the possibility of independent characterization, as well as independent optimization, of the gain and passive chips and their spatial separation providing good heat dispersion. Further on, the mode matching between the gain and the silicon PIC can be engineered through the implementation of spot-size converters (SSC) [61,62] to relax the alignment procedures, or implementing new integration approaches such as transfer-printing (TP) [62,63], briefly discussed at the end of this review.

The relatively high output power, independent optimization of the gain and passive components, and layout flexibility offered by HECLs make these devices a valid solution for energy efficient optical interconnects. They also offer a high degree of components customization that contributes to their employment in other fields such as sensing and biomedical – for example in the case of Fourier domain Mode-Locked Lasers (FDMLs), discussed later in this review as a unique example of HECL versatility.

5. Thermally-stable distributed Bragg reflector-based HECL on silicon nitride (SiN)

Current coarse Wavelength Division Multiplexing (CWDM) optical links employed by data centres use Distributed Bragg Reflector (DBR) lasers and external silicon modulators [63]. This unavoidably leads to laser stability and power consumption issues due to the high thermo-optic coefficient (TOC) of silicon [64]. This sensitivity requires active cooling [65] of the laser and wide channel spacings [66] to avoid channel cross-talk, particularly as datacentres exhibit wide temperature ranges. To counteract the detrimental effects of thermal drifts many device configurations have been proposed in literature, ranging from loop mirrors and Mach-Zehnder interferometers used as thermally tuned frequency discriminators [67,68], to MRR feedback controls [29]. However, thermal tuning is very power consuming and silicon rings do not provide athermal references, rendering these solutions incapable to deal with the thermal stability issue of these class of lasers.

For this reason, research interest has recently started to shift towards other silicon-based platforms such as Si_3N_4 on Insulator, which allows for good optical confinement, relatively low losses, and lower free-carrier absorption. More importantly the much lower TOC of Si_3N_4 compared to Si on SOI platforms [69] unlocks the possibility of greatly improved laser thermal stability – as demonstrated in [70].

Indeed in [70], the first thermally stable operation of a HECL based on Si_3N_4 DBRs has been achieved exploiting the material intrinsic thermo-optic properties, without the need for active cooling or feedback controls, in a wide range of temperatures (from 20°C to 80°C). This demonstrated the hybrid laser advantage of being composed of different materials (with different

Optical Materials EXPRESS

TOCs) which enable the possibility of athermal operation – a feat that single material devices, such as monolithic lasers, cannot achieve.

This HECL under discussion used a commercially available rSOA based on AlInGaAs, whose Al^{3+} ions contained in the QWs deepen the potential well and obstruct carrier leakage at elevated temperatures, thus facilitating higher temperature operation [71]. The rSOA was butt-coupled to a Si_3N_4 waveguide on which Bragg gratings had been patterned with DUV lithography – as shown by the schematics **in** Fig. 3(b). In this configuration, the passive and active chips were optimized independently and the Si_3N_4 waveguide was tailored to better match the rSOA optical mode, achieving a relatively high coupling efficiency between the two components of 80% with a misalignment tolerance of ±1 μm (as shown in Fig. 4(b)).

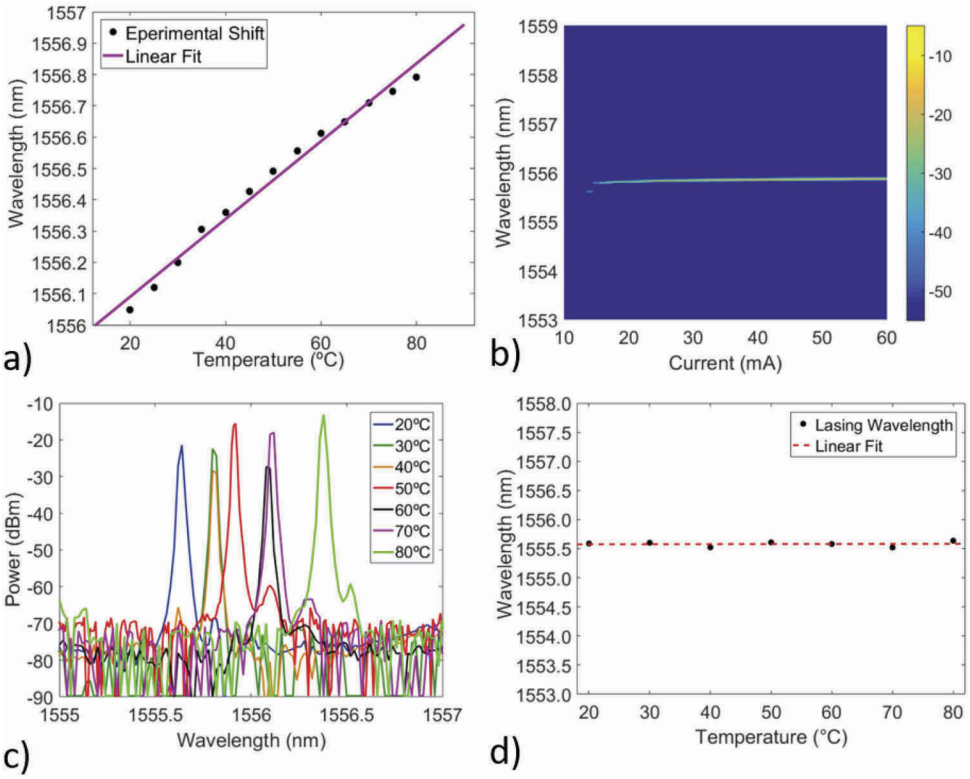

Fig. 4. a) resonance wavelength shift of a SiN DBR with temperature, showing a temperature stability of 12 pm/°C, b) False colour plot of the optical spectrum of the HECL based of the SiN DBR, averaged in time, with the increasing driving current, showing a lasing wavelength stability of ~55 mA, c) spectra of the laser at different operating temperature, showing a lasing wavelength shift <200 GHz in a 60°C temperature difference and d) linear fit superimposed to the lasing wavelength shift with temperature.

Thermo-optic measurements conducted on the Si_3N_4 chip in the work under consideration show a low thermal sensitivity of the Bragg reflectors of 12.4 pm/∘C, also depicted here in Fig. 4(b) resulting in a measured Si_3N_4 TOC of $1.62 * 10^{-5}$RIU/∘C and greatly contributing to the laser improved thermal stability – Fig. 4(d) The characteristics of the resulting hybrid laser based on the Si_3N_4 DBRs also show a low current threshold of 10 mA and a wide mode-hop free single-mode lasing regime of ~50 mA, while maintaining power outputs in the range of mWs, compatible with the power requirements of current WDM technology. The laser in question has shown a wavelength thermal stability of 2.7 pm/∘C, corresponding to a thermal drift well

Optical Materials EXPRESS

below the 200 GHz and 400 GHz channel spacing standards in CWDM, potentially enabling the employment of arrays of these devices as compact transmitters in datacentres, without active cooling.

The replacement of the DBRs in Si_3N_4 with resonators, such as 1D and 2D photonic crystal cavities, with higher Q factors and much smaller footprints compared to gratings, could lead to further improved performances in terms of accurate lasing wavelength control and wider mode-hop-free regime.

6. Thermo-optic dynamics of 2D photonic crystal cavities

The most unique characteristic of PhC cavities is their ability to tightly confine light at wavelength-scale footprints, leading to a greatly enhanced light-matter interaction useful for the exploitation of the small non-linearities of silicon [24]. This microcavity effect is even more relevant for the thermo-optic behaviour of the component (i.e., the interaction between the confined light with the thermal and optical properties of the PhC cavity) as significant optical power gets absorbed in the very small volumes of the structured material. If the PhC is included in a laser cavity, the high intracavity power further enhances this effect, as will be discussed in greater detail in Section 7. Therefore, the study of the thermo-optic dynamics involved in PhC cavities becomes paramount to understand their response and loss mechanisms, especially with the relatively high powers they are subjected to in a laser configuration like HECLs. It follows that to use 2D photonic crystals effectively in HECLs (and in general as integrated photonic components) it is necessary to fully understand the dynamics underlying PhC resonators, before diving into the discussion regarding PhC cavity-based HECLs.

In the near MIR/C-band, the dynamics of optically pumped silicon microcavities is dependent on their thermal response, dominated by two phenomena:

- the heat generation related to optical absorption – either through defect/surface states, or through absorptive non-linearities such as two photon absorption (TPA) and free carrier absorption (FCA)

- the heat transfer through the chip, following Fourier's Law of Heat Conduction.

The high Q-factor and surface to volume ratios (Q/V and S/V respectively) of microcavities also leads to enhanced thermal effects as thermal processes and heat dissipation are size dependent, rendering their effect more pronounced on the PhC cavity dynamics.

A first principles model to fully describe the thermo-optic nonlinear dynamics of optically pumped silicon PhC cavities (shown in Fig. 5(b)) is reported in [72]. In this model, the space-time temperature distribution of an integrated PhC cavity and chip is calculated – shown by the thermal volume expansion in time depicted as enlarging warm-coloured ellipses in Fig. 5(b). This represents the material progressively heating up in time by a laser beam incident on the chip. In this way the possibility is unlocked to calculate a realistic representation of the pump-cavity system's response, demonstrated by the good match with the experimentally measured dynamics on all relevant timescales.

The optically pumped system is subjected to three main phenomena: the light trapped in the microcavity is partially absorbed by defect/surface states (linear absorption), two-photon absorption (TPA) and free carrier absorption (FCA). Subsequently, the carriers generated by TPA and FCA relax transferring energy to the material atomic lattice as heat, which in turn is dissipated through heat conduction mechanisms. The FCA decreases the refractive index of the material through plasma dispersion effect, while the heat generated by all absorption processes increases it through thermo-optic effect. The concurrence of these opposite effects allows the pump-microcavity system to reach stable and unstable equilibrium states.

The time-varying linear and non-linear response of the 2D PhC is, therefore, governed by the generation and transfer of the heat related to the absorption of the optical power coupled

Optical Materials EXPRESS

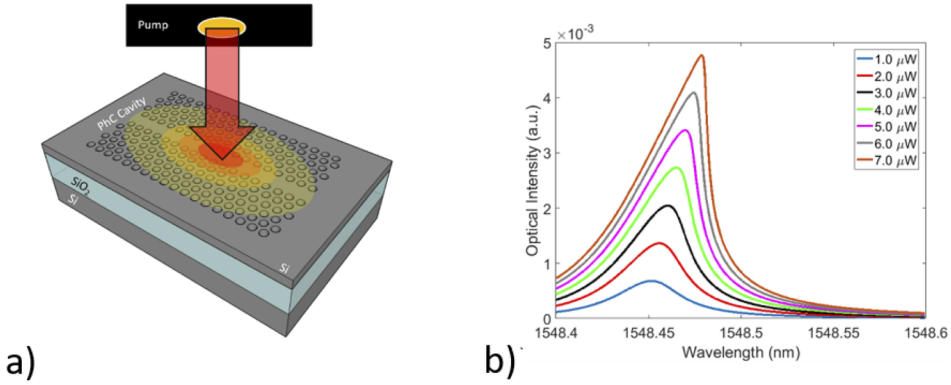

Fig. 5. a) schematics of the chip-integrated 2D PhC cavity, where the warm-coloured concentric ellipses represent the portion of material progressively heating up with time due to the optical pumping. The model calculates the temperature distribution in space and time at each time step, dividing the material in elliptical increments, b) plot of the calculated dynamic response of a silicon PhC Dispersion-Adaptive cavity generated by sweeping the wavelength of the exciting optical pump.

into the cavity. This can be realistically described by time-dependent classical rate equations for the optical energy, the free-carrier number density, the thermal energy density and the heat loss rate [72], used in combination with the Laplacian heat transfer equations that outline the system temperature distribution in both time and space. Fig. 5(b) shows the calculated response of a PhC cavity (in this case the dispersion adapted design [37–40]) obtained by sweeping the wavelength of the exciting pump laser.

A deep understanding of the thermo-optic dynamics dominating the response of these microcavities becomes of considerable importance to predict and tailor the behaviour of these components for a vast range of applications, such as in the case of self-tuning and power tuning mechanisms in PhC-based HECLs – described at the end of Section 7.

7. 2D photonic crystal cavity-based HECL on crystalline silicon platform and power-tuning

Following up on previous demonstrations of such hybrid, HECLs [31], [60], and especially those using DBRs [26], we present in this section an EC laser architecture that utilizes a silicon PhC cavity-based resonant reflector [73], which allows for reduced footprint, high side-mode suppression ratio (SMSR), and high-precision wavelength control. More specifically, the Si-based mirror of choice is a low refractive index (e.g., polymer or SiN_x) waveguide vertically coupled to an oxide-clad 2D PhC cavity on SOI. The top oxide cladding of the cavity acts simultaneously as an accommodating platform for the waveguide and as a buffer layer, as light can evanescently couple through it between the waveguide mode and the cavity mode at the resonant frequency of the PhC [74] (Fig. 6). The vertical coupling configuration allows for lower insertion and transmission losses, isolation, and maximization of the area available for electronic circuitry on Si and offers the possibility of precisely controlling the coupling between the bus waveguide and the Si PhC cavity.

The functionality of the system as a resonant mirror stems from the narrow-band wavelength-selective optical feedback provided by the backward propagating light component that is coupled into the waveguide from the PhC cavity [38]. A conceptual representation of the system's function is given in [Fig. 7]. Under weak coupling assumption, the transmittance and reflectance

Optical Materials EXPRESS

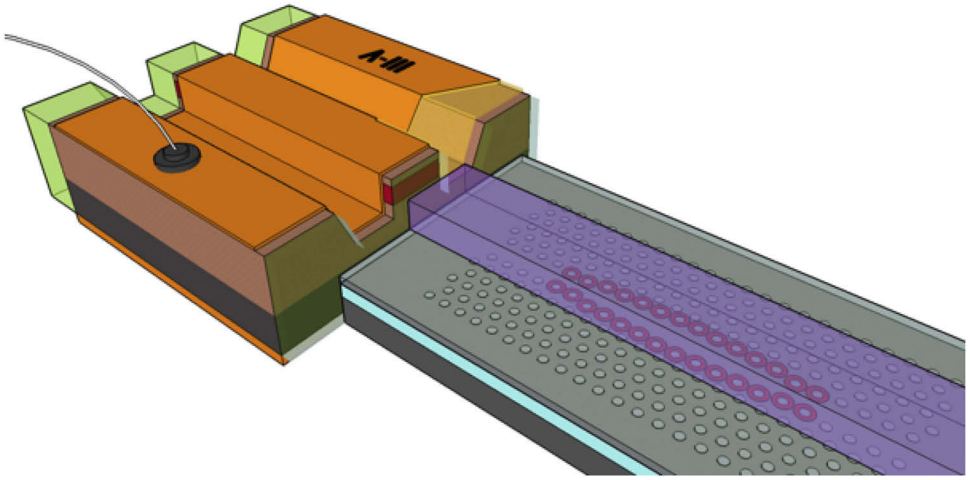

Fig. 6. Schematics of the HECL based on vertically coupled Photonic Crystal Cavity, in which an RSOA (in orange) the SU8 polymer waveguide is represented in purple and the actual silicon PhC cavity in grey.

in the waveguide at resonance are given by [74]:

$$T = \frac{Q_{total}^2}{Q_{cavity}^2} \qquad R = \frac{Q_{total}^2}{Q_{coupling}^2}. \tag{3}$$

where Q_{cavity} is the intrinsic Q-factor of the PhC cavity, $Q_{coupling}$ describes the coupling between the waveguide and the cavity, and Q_{total} is the overall Q-factor of the system, given by

$$\frac{1}{Q_{total}} = \frac{1}{Q_{cavity}} + \frac{1}{Q_{coupling}}. \tag{4}$$

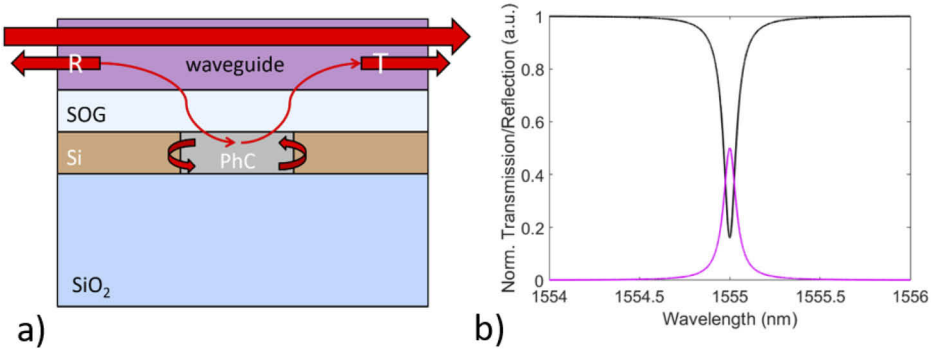

Fig. 7. (a) 2D schematics of a dielectric bus waveguide vertically coupled to a PhC cavity at the resonant condition. The red arrows represent light propagating in the waveguide, coupling in the cavity, being confined and consequently coupling back into the waveguide in backward and forward directions. (b) Normalized transmission (magenta) and normalized reflection (black) for the vertically waveguide-PhC cavity system, with intrinsic Q-factor, Q0, of 40000 and coupling Q-factor, Qc, of 20000.

An oxide-clad PhC cavity design is selected for higher compatibility with the various SiP technology platforms, but also because the oxide cladding offers improved mechanical and

Optical Materials EXPRESS

thermal stability compared to silicon membranes [75], [76] without inhibiting the achievement of Q-factors which are high enough ($>10^6$) for most practical applications [77] For the SiP reflector chip, an oxide-clad Dispersion Adapted (DA) Si PhC cavity [78,79] was vertically coupled to an SU8 polymer bus waveguide, as described in [74]. The waveguide facets were finally coated with an AR layer. A conceptual representation of the above-described laser configuration is shown in Fig. 6.

To demonstrate lasing with low threshold current, it was necessary to maximize the power coupling between the rSOA and the polymer waveguide. The optical mode overlap between the two waveguides determines the highest achievable coupling efficiency. Finite Difference Eigen-mode (FDE) simulations were performed using FIMMWAVE and FIMMPROP by Photon Design. The simulated modal area of the fundamental TE mode of the bus waveguide was found to be 4.2 μm^2, which is a close match to the rSOA waveguide's TE modal area of 4.557 μm^2, resulting in a nominal coupling efficiency of 85%. The high coupling efficiency between the rSOA and the bus waveguide resulted in threshold currents in the 10-25 mA range at an optimal alignment position. Fig. 8 show the simulated and experimentally measured power coupling between the rSOA and the bus waveguide. During the experimental measurements, the SiP chip was kept at a fixed position and the rSOA waveguide was moved to different horizontal and vertical position relatively to the centre of the bus waveguide. Given the large modal area of the polymer waveguide, excess coupling losses of < 0.5 dB were measured for +/- 0.5 μm vertical and horizontal misalignments from the maximum coupling position.

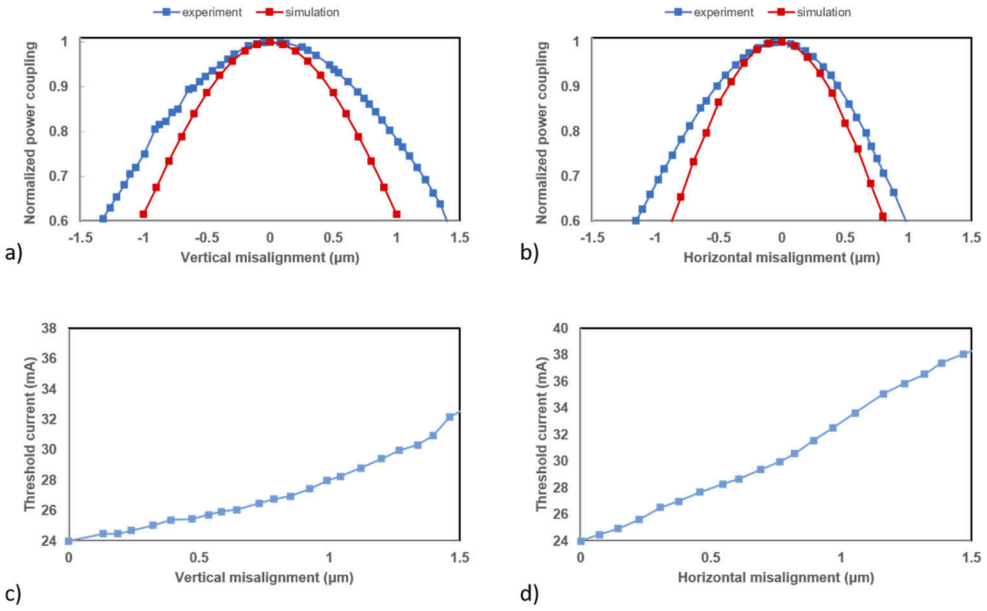

Fig. 8. Experimental (blue) and simulated (red) normalized power coupling coefficient, as a function of (a) horizontal (y-axis) and (b) vertical (x-axis) misalignment of the rSOA from the (SU8) bus waveguide on the reflector chip, relative to the optimal coupling position. Threshold current as a function of (c) horizontal and (d) vertical rSOA-waveguide offset, relative to the optimal coupling position.

Output powers of several mW were measured in every case, with a maximum waveguide-coupled wall-plug efficiency of 8% at 40 mA. Fig. 8 shows the data obtained for an indicative device. The measured side-mode suppression ratio (SMSR) was determined to be in the excess of 40 dB over the full considered current range, with a maximum value of 50 dB.

Optical Materials EXPRESS

The use of a PhC cavity in the Si reflector results in very high stored energy densities (in the PhC cavity), and therefore in increased local heat dissipation in the resonator's small modal volume, due to nonlinear absorption in silicon [72,73], as explained in Section 6. As the PhC cavity temperature sets its resonant wavelength, and the energy stored in the PhC cavity is proportional to the intra-cavity power in the laser cavity, the emitted wavelength of the examined HECL configuration is a sensitive function of the laser power. Based on that, the tuning of the lasing wavelength in such a HECL configuration through the laser output power was proposed in [73].

Wavelength stability in this laser configuration can be realized for uncooled operation by balancing the variation in the ambient temperature with changes in the PhC cavity temperature through heating caused by carrier recombination. If the laser power is appropriately decreased as higher operating temperatures are reached, the two effects can be adjusted to cancel each other out, giving a zero-net shift of the emitted wavelength. This inherent passive mechanism (referred to as power tuning) was exploited to balance ambient temperature changes with controlled absorptive heating in the PhC cavity. Using power tuning, a lasing wavelength stability of +/- 0.38 nm over a temperature range of 20-80°C under uncooled operation was demonstrated [73].

8. 2D photonic crystal cavity-based HECL on an amorphous silicon (a:Si) platform

The silicon on insulator platform is not ideal for electronics-photonics integration as the thick buried oxide required for the optical confinement of SiP components is detrimental to the dissipation of the heat generated by the operation of transistor, rendering the electronic-photonic packaging extremely difficult on the same platform. This translates into the need for laterally or vertically integrated solutions in which the optical components are fabricated onto deposited island of silicon-based materials on thick silica, embedded into the bulk silicon wafer (where the electronics lie), thus excluding the possibility to employ the only-grown c:Si. This becomes relevant in view of further reducing optical interconnect energy consumption and increasing their data rates, where new schemes requiring photonic routing and processing electronics packaged on the same substrate are becoming popular [5]. To face this challenge, interest has been directed to CMOS compatible materials with optical properties similar to c:Si, such as amorphous silicon (a:Si), with a refractive index as high as c:Si offering good optical confinement and waveguiding.

Despite a:Si showing higher propagation losses at telecom wavelengths due to dangling Silicon bonds (partially resolved by H^+ implantation), it offers the possibility to be deposited at low temperature (<300°C) directly onto other layers (i.e., processing electronics) [9], without affecting the performances of transistor [7], unlocking the possibility of CMOS back-end-of-the-line processing. Recent optimization of deposited hydrogenated a:Si has led to high performance waveguides, multiplexers, grating couplers, MZIs, MRRs and power splitters ([10], [11]). However, the full potential of a:Si can be unleashed by its implementation as passive chip in HECLs, rendering this type of laser fully compatible with electronic-photonic integration on the same substrate.

In this section, the first demonstration of a 2D PhC HECL on a:Si platform is summarized with its lasing characteristics [40]. The device comprises a pig-tailed semiconductor optical amplifier (SOA) acting as gain, coupled on one side to a 98% fibre retro-reflector (broadband mirror) and on the other side to an SU8 polymer waveguide patterned on top of the passive chip, with is in turn vertically coupled to a DA PhC cavity etched in a 220nm thick layer of PECVD a:Si deposited at 350°C on 2100 nm of silica (Fig. 9(b)). The vertically-coupled 2D PhC acts as wavelength selective mirror, as in the case of its c:Si-based HECL counterpart. Moreover, the SOA in pig-tailed configuration unlocks the possibility to implement long chains of optical fibres between the retro-reflector and the PhC resonator, allowing control on the FSR of the long laser cavity, and ring laser configurations.

Optical Materials EXPRESS

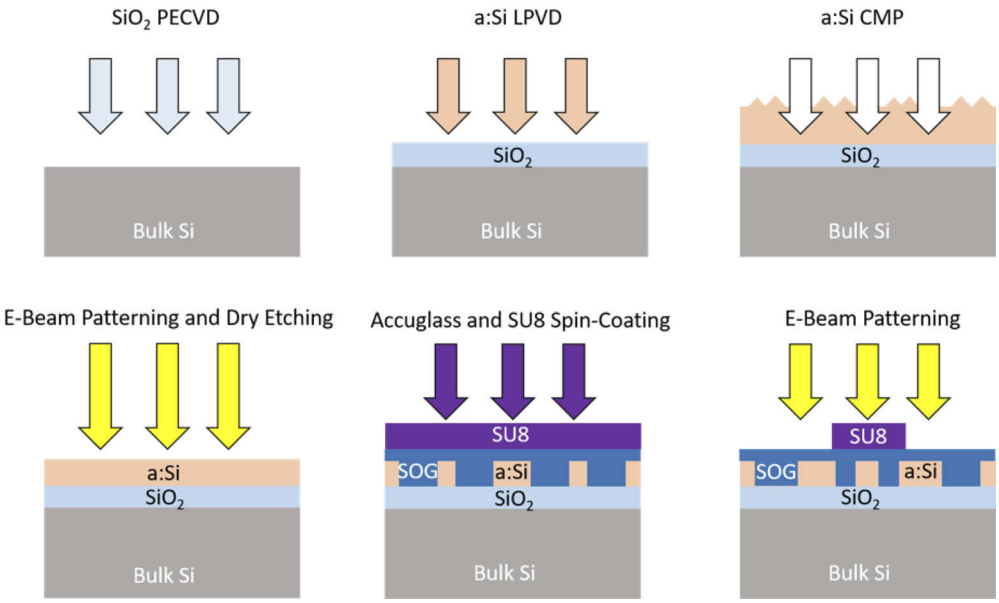

Fig. 9. Processing workflow for the deposition and polishing of the amorphous Silicon (a:Si) to obtain optically optimized PhC resonators.

Results obtained in [40] indicate low propagation losses affecting this type of platform and are the first demonstration of both lithographic control of the PhC cavity on a:Si and single-mode lasing achieved on this platform (as shown in Fig. 10(b)). In Fig. 10(b) the lasing spectrum of the device is being superimposed on the same spectrum below lasing threshold, highlighting lasing wavelength selectivity shown by the coincidence of the 2D PhC cavity resonance and the laser line. Fig. 10(b) shows the L-I characteristics of the a:Si-based HECL, characterized by a lasing threshold of 27 mA and output power in the order of tens of mWs with the pig-tailed SOA in the 11m-long cavity configuration.

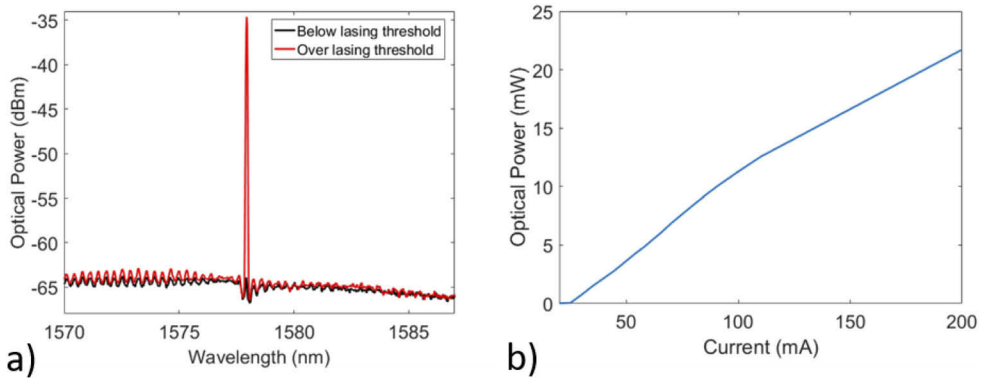

Fig. 10. a) spectrum of the a:Si PhC cavity below lasing threshold (black) showing the resonance dip in transmission, overlapped with the same spectrum at higher driving current (over lasing threshold), showing the laser line in correspondence to the PhC cavity resonance, b) optical power output of the a:Si PhC based HECL against driving current

The results achieved in [40] demonstrate the potential to develop compact, cost-effective, high-performance semiconductor lasers in HECL configuration on the a:Si platform, which can

Optical Materials EXPRESS

be easily integrated on the electronic processing layer of microprocessors for the next generation of fully CMOS optical interconnects.

9. Direct frequency modulation of photonic crystal laser: a proof-of-principle for datacomms applications

Silicon based resonant modulators take advantage of the strong light confinement and high Q-factor of the resonator which enhances the electro-optic effect upon modulation of the carrier distribution. This results in optical modulators which demonstrate a low switching energy and high extinction ratio with a small device footprint – essential attributes to reduce energy consumption costs for optical interconnects. This, along with CMOS compatibility gives a high manufacturing yield, making them one of the leading technologies in short reach datacommunications. Many configurations of silicon based resonant modulators have been reported in recent years, such as microring resonators [80–83], racetrack resonators [84,85], microdisks [86,87], and 2D PhCs [37,88]. However, fabrication imperfections and temperature variations can create a mismatch in wavelength between the laser source and the modulator resonance, requiring tuning elements and control circuitry which increases power consumption.

In contrast the emitted wavelength of HECL is determined by the resonant wavelength of the PhC cavity when employed in the laser cavity. In these configurations, the requirement to match the emitted laser wavelength and filter transmission wavelength is eliminated, further reducing device complexity and energy consumption. PhC cavities produce a narrowband reflection peak with low insertion loss leading to low threshold currents. As such, the devices in the previous sections have demonstrated compact, energy efficient, low threshold and high SMSR single mode HECLs based on PhCs. Given the small volume of the PhC cavity, a very low capacitance exists whereby directly modulating only this section can produce GHz modulation speeds [37]. This contrasts with traditional modulation approaches such as the DFB laser where direct modulation is applied to the entire laser cavity, resulting in a larger capacitance and thus limiting the modulation speeds which can be achieved.

Frequency modulation of the hybrid PhC laser (Fig. 11(a)) was achieved by directly modulating the reflectance phase of the PhC cavity resonant reflector [39]. Owing to the short Fabry-Perot laser cavity length, one longitudinal mode lies within the narrowband reflection peak of the PhC cavity. Tuning of the reflection peak then consequently tunes the lasing mode (Fig. 11(b)) based on the phase matching condition as $2kL + \phi_r = 2\pi m$, where k is the propagation phase, L is the length of the cavity, and m is an integer. ϕ_r is the reflection phase of the narrowband reflector incorporated with the laser cavity propagation phase and only ϕ_r is altered. The linear approximation for the tracking of the lasing mode relative to the reflection peak has been derived in [39] and is given by:

$$\Delta v = \Delta \mathrm{F} \left[\frac{1}{1 + \frac{2\pi\Gamma}{FSR}} \right]. \tag{5}$$

where $\Delta\nu$ is the lasing frequency shift, ΔF is the reflector frequency shift, Γ is the bandwidth of the reflector and FSR is the Free Spectral Range of the laser cavity.

Tuning of the reflectance band can be achieved by changing the resonance wavelength of the PhC cavity. Based on the electro-optic or thermo-optic effect in silicon, injection/depletion of carriers or local heating of the PhC cavity will modify the material refractive index. This shifts the resonance wavelength and in the hybrid laser configuration, tunes the reflectance peak to give laser wavelength tuning. The gain bias current can remain fixed and the modulation current be applied only to the small volume of the PhC cavity. Doping of the PhC cavity and the addition of a p-n junction allows for the injection/depletion of carriers. Carrier induced refractive index change of a doped p-n junction on a 2D silicon PhC cavity has been demonstrated [37] showing modulation speeds reaching 1 Gbit/s with a switching energy of 1.6 fJ.

Optical Materials EXPRESS

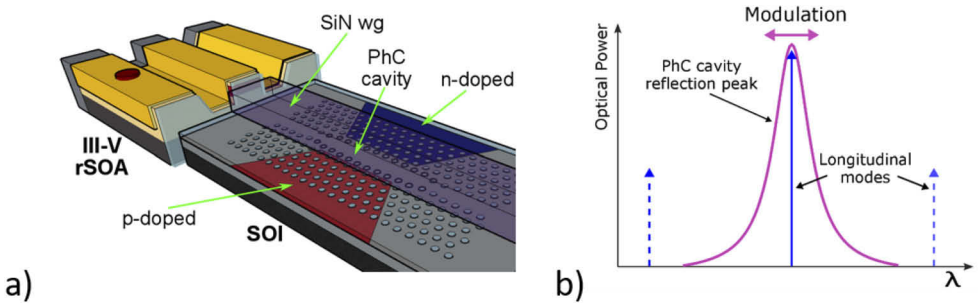

Fig. 11. (a) Laser configuration with rSOA butt-coupled to SOI chip comprising a doped p-n junction embedded in the PhC cavity. Bias current on rSOA is fixed with modulation current applied to the p-n junction. (b) One longitudinal mode lies within the reflectance band of the PhC cavity and modulation of the reflectance peak consequently modulates the lasing mode.

The HECL used the same configuration as described in Section [7] by butt-coupling the rSOA waveguide to the waveguide on the silicon chip which was vertically coupled to the PhC cavity. In this configuration, a low refractive index Si_3N_4 waveguide was employed and the PhC cavity was embedded in a doped p-n junction. The SiN allowed for good mode matching with the rSOA waveguide mode and the SiN layer gives the possibility for integration of other devices such as multiplexer/demultiplexers.

The 2D silicon PhC is fabricated as described in Section [7] with the addition of four different levels of doping used to create a p-n junction. The low doped p-n junction is designed to overlap with the DA cavity to achieve maximum electro-optic efficiency. The p-n junction is created by implantation of boron and phosphorous ions to realise the targeted doping concentration of $\sim 10^{19}$ cm^{-3}. Further details on fabrication of the p-n junction can be found in [37].

The fabricated devices had a resistance of 0.5 kΩ and by applying forward bias to the p-n junction, the thermo-optic effect in silicon was exploited. Therefore, for the experiments described here, the p-n junction operated as an efficient microheater giving a red-shift of the resonance wavelength achieved by local heating in the PhC cavity.

In the EC laser configuration, the rSOA current was kept fixed at 50 mA giving a single mode lasing wavelength with an SMSR of ~45 dB. Using a bias-tee and waveform generator, a 2.9-3.7 V 10 kHz triangular wave modulation was applied to the p-n junction (Fig. 12(b)) on the PhC cavity via needle probes. In order to capture the laser frequency modulation, a heterodyne measurement was undertaken. A narrow linewidth tunable laser source (TLS) was set at a fixed wavelength close to the lasing wavelength, then mixed with the laser output and sent to a 33 GHz photodetector generating a beating intensity on the oscilloscope. Post-processing of the time trace involved employing a sliding window FFT over a series of time segments to compute the beating frequency for each segment. This allowed for measurement of the time varying lasing frequency as the modulation was applied to the p-n junction thus, capturing the direct frequency modulation of the hybrid laser (Fig. 14(b)).

The modulation depth $\Delta\nu$ (i.e. lasing frequency shift) was ~6.5 GHz for this drive signal range and this decreased with increasing modulation frequency due to the frequency roll-off of the p-n junction and the limitations of thermal tuning. However, improvements in fabrication of the p-n junction are expected to increase the modulation efficiency. Another limitation on the modulation depth is the relationship of the lasing frequency shift vs. reflector shift. As shown in **Eq. (5)**, a laser cavity with a large FSR (short cavity length) and a narrow bandwidth reflector will result in a larger frequency shift for a given reflector shift. These are considerations for the laser cavity design in order to improve the frequency tuning efficiency. Finally to note,

Optical Materials EXPRESS

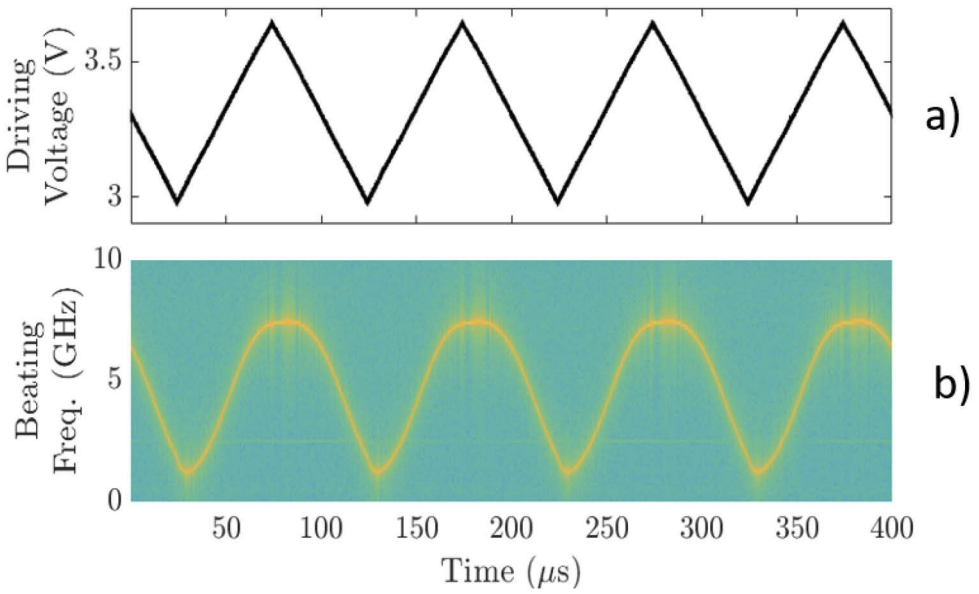

Fig. 12. (a) Driving voltage to p-n junction. (b) Captured laser frequency modulation given by the beating frequency between the laser signal and mixed with the fixed TLS signal.

operation here was in the single mode regime, therefore the maximum $\Delta\nu$ which can be achieved without mode-hopping to the adjacent longitudinal mode is limited by the laser cavity FSR. The next section will demonstrate a hybrid laser configuration to extend the continuous tuning range beyond this single mode FSR limitation.

10. Fourier domain mode-locked (FDML) laser based on photonic crystal HECL

An extension of the applicability of the tunable reflectance band of the PhC cavity was presented in [88] with a novel configuration of an FDML laser. The FDML laser is a specific configuration of a wavelength swept laser to maximise wavelength sweep range and speed while maintaining high output power [89]. These mostly find application in the imaging technique known as swept source Optical Coherence Tomography (SS-OCT).

Many swept source lasers consist of a broadband gain medium and a tunable optical bandpass filter to produce narrowband wavelength sweeps [9192–94]. A common limitation on sweep speed is the so-called post-filtering limit [87], consisting in the filter being swept by more than the filter width during the cavity roundtrip period. The FDML configuration overcomes this limit by sweeping the filter at a period synchronous to the roundtrip time of the cavity as $f_{mod} = m/T$, where f_{mod} is the filter modulation frequency, T is the roundtrip time and m is an integer [90]. A full sweep is optically stored in the cavity which overcomes the restriction of cavity build-up time as lasing does not need to build up from spontaneous emission with each sweep as with other swept sources, meaning the only limitation on sweep speed is the speed of the filter. A large cavity length is usually required to facilitate synchronisation of the roundtrip time and filter speed but the principle of FDML can be scaled to any cavity length solely depending on the maximum filter speed achievable.

The previous section demonstrated the hybrid PhC laser with a short laser cavity length where one longitudinal mode lay within the reflectance band of the PhC cavity. A proof-of-concept FDML laser using the same PhC device with the doped p-n junction was demonstrated [90] by exploiting the tunable reflectance spectrum of the PhC cavity. The length of the laser cavity was

Optical Materials EXPRESS

significantly longer with the addition of a 2 km fibre delay line resulting in ~10^6 longitudinal modes within the reflector bandwidth. Along with the 2 km fiber delay, the laser cavity consisted of a fibre retro-reflector, a fibre pig-tailed Kamelian SOA, a polarisation controller, and a lensed fibre to couple the light into the waveguide vertically coupled to the PhC cavity reflector (Fig. 13). Measurements were taken from an intra-cavity splitter sent to an isolator and split to an OSA and oscilloscope. Applying the principle of FDML operation, the modulation frequency applied to the p-n junction was equal to the inverse of the roundtrip time of the laser cavity.

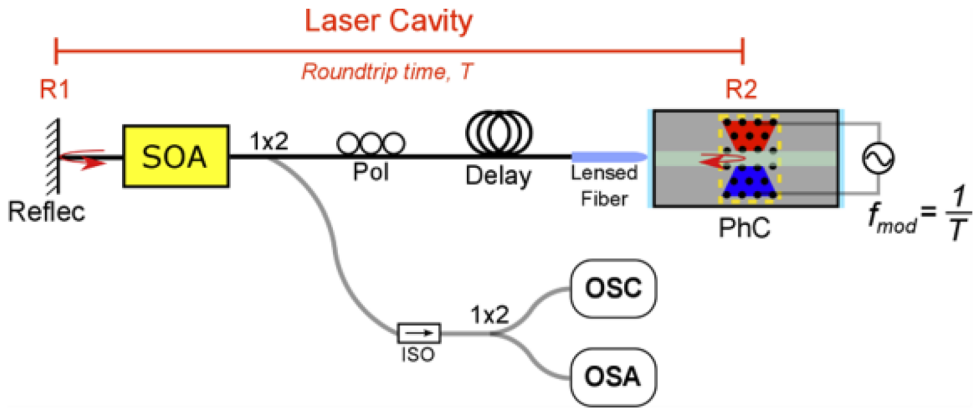

Fig. 13. FDML PhC laser configuration and experimental set-up.

Firstly, the laser characteristics with a static reflector as a function of SOA current were examined with no voltage applied to the p-n junction. The laser had a threshold of 35 mA and the LI curve showed a slope efficiency of 0.14 mW/mA. As shown in Fig. 14(a), just above threshold, the spectrum showed a single peak. However, multiple longitudinal modes were expected within this peak as the laser cavity FSR was ~1.2 fm. With further increase of bias current, more longitudinal mode began to lase and the full bandwidth of the reflector could be seen. The fringes on the spectrum were due to the parasitic reflections from the chip facet to the PhC cavity. The intensity on the oscilloscope showed unstable dynamics on both the nanosecond and seconds timescales and large power fluctuations were observed as expected for multimode lasers [95]. With fixed current on the SOA of 70 mA, DC voltage steps were applied to the p-n junction via needle probes and a red-shift of the lasing spectrum was observed again, as a result of the

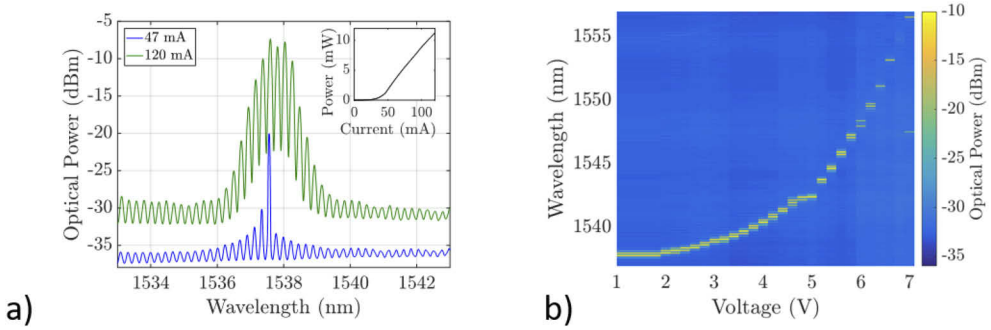

Fig. 14. a) Optical spectrum of lasing characteristics with a static reflector and increase of SOA bias current. Inset: LI curve. b) Colourmap of optical spectrum with fixed SOA bias at 70 mA and DC voltage steps applied to the p-n junction.

Optical Materials EXPRESS

thermo-optic effect in silicon. Fig. 14(b) shows a shift of ~18 nm for 7 V applied to the p-n junction.

Using a bias-tee and a function generator, a sine wave of 2.8-5 V was applied to the p-n junction. The roundtrip time of the Fabry-Perot laser cavity, $T = 2nL/c$, was estimated to be 20 µs with $n_{glass} = 1.5$ and $L = 2$ km. Hence, the modulation frequency, $f_{mod} = 1/T$ was calculated as 50 kHz. Further fine tuning of the modulation frequency resulted in a stable swept wavelength spectrum at 50.35 kHz with a range of ~4 nm (Fig. 15). The spectrum again shows fringes as a result of parasitic reflections from the PhC cavity to chip facet. A reduction in the fringes can be achieved by using chips with angled waveguides and application of anti-reflection coatings.

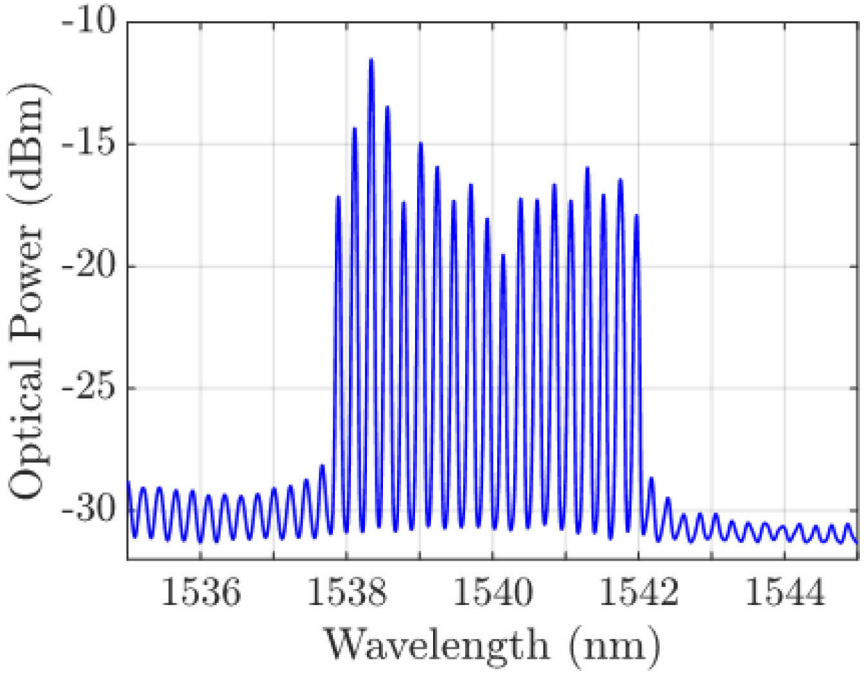

Fig. 15. (a) Optical spectrum of swept wavelength in stable FDML operation.

The output intensity showed a periodic amplitude envelope over the swept wavelength range with stable average output power over time. The sweeping instantaneous frequency was calculated using a self-heterodyne interferometric measurement technique [96]. This allowed for direct measurement of the laser phase and subsequent post processing was undertaken to calculate the instantaneous frequency. This confirmed the continuous swept frequency in the FDML regime when the reflector modulation period was matched to the inverse cavity roundtrip time.

The utilisation of an on-chip akinetic tunable reflector opens the path for a compact integrated FDML laser. The FDML laser was in a Fabry-Perot linear configuration therefore, no isolators were required for a ring laser cavity, which would be a barrier to on-chip integration. In devices similar to the PhC p-n modulators used here, maximum modulation speeds of 0.5 GHz have been shown [37] which is far beyond the sweep rates of the mechanical filters which are typically employed in FDML lasers. The cavity length could then be on the order of 10s of centimetres to match the inverse of the cavity roundtrip time. However again, the steep frequency roll-off of these devices reduces the sweep range with increasing sweep speed. Improvement in fabrication of the modulators will enable larger sweep ranges with increased sweep speeds while having the potential to develop a fully integrated FDML laser.

Optical Materials EXPRESS

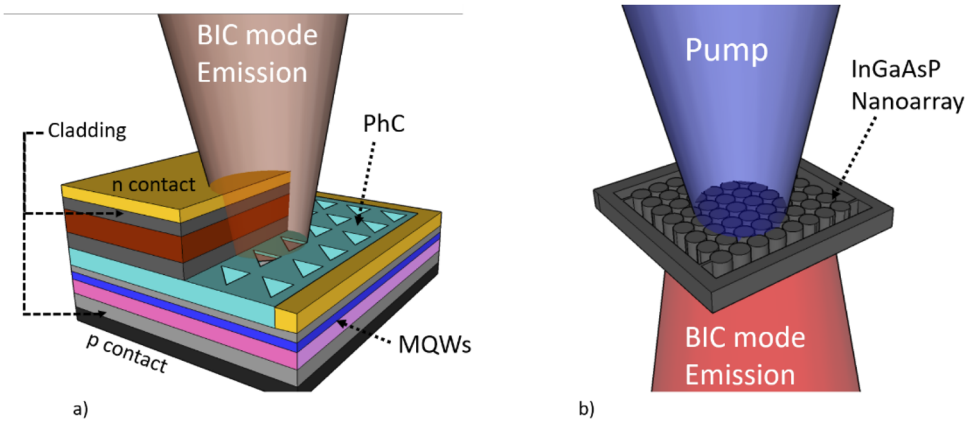

Fig. 16. (a) Schematics of a PCSEL based on symmetry-protected quasi-BIC mode. The quasi-BIC mode is generated due to the breaking of the 180° rotational symmetry operated by the triangular air-holes of the PhC. (b) Schematics of the suspended optically pumped InGaAsP MQWs nano-resonator array, as in [107], in which the pump beam is represented in blue and the resonance-trapped BIC laser mode is represented in red.

11. Bound-in-continuum (BIC) states for photonic crystal lasing

Recently, considerable research effort has been directed towards the development of photonic devices, including semiconductor lasers, that exploit the high Q-factor properties of Bound-In-Continuum (BIC) states. Typically, an optical mode is trapped in a defect in a periodic medium (like PhC cavities) due to the lack of radiating modes extending outside of the defect for it to couple to – a direct effect of the photonic bandgap. In contrast, the generation of BIC states, arises from the fact that an optical mode confined in certain media (e.g., periodic structures), despite the presence of extending modes outside of the optical trap (i.e., the trapped mode falling in the continuum spectrum of allowed propagating modes), eliminates its own radiation in those extended modes through interference phenomena. This alternative but fundamental wave confinement possibility, firstly postulated by von Neumann and Wigner [97], can achieved through a plethora of mechanisms [98,99], ranging from symmetric properties to parameter tuning. Periodic structures can easily exhibit BIC states, thanks to their symmetry and engineerable periodic potential [100], rendering them popular candidates for BIC-based semiconductor lasers.

A class of such lasers is represented by various configurations of surface-emitting lasers based on symmetry-protected BICs, in which the BIC mode is restricted to high symmetry points of the PhC reciprocal lattice (typically at the Γ point). The principle was first demonstrated in surface-emitting distributed feedback lasers [101] by suppressing radiation along the direction normal to the device surface, and later by 2D PhC based PCSELs [41,43], in which the BIC 2D periodicity led to different complex lasing patterns (as discussed in [13,14] and in Section 2) and low-threshold lasing in optofluidic systems based on organic molecules cladding macroscopic PhC slabs [102]. Yet, the suppression of radiation along the direction normal to the emitting surface, despite allowing low lasing thresholds, greatly limits the lasing output power, leading to the development of different PhC configurations to solve this issue. The most recent solutions involve PhC designs that intentionally break rotational symmetry, such in the case of triangular air-holes PhCs [43], to allow controlled leakage of radiation along the normal direction, leading to continuous-wave lasing emission at powers up to 1.5 W at room temperature while maintaining high beam quality and a relatively low threshold – thus unlocking the possibility to employ them in lens-free applications in laser medicine, material processing and sensing. Moreover, the topological charges of the BIC modes in PCSELs enable the generation of vector beams [15,103],

Optical Materials EXPRESS

potentially employable in compact particle accelerators, optical trapping, laser machining and ultra-resolved microscopy [104].

A more recent class of bound-in-continuum state-based lasers is represented by devices that exploit resonance-trapped BIC modes, which are characterised by ideal infinite Q-factors on resonance while maintaining very high Q-factors off-resonance (compared to the rapid decay in confinement in symmetry-protected BICs), are not limited only to high symmetry points of the lattice and are therefore less affected by symmetry breaking [105]. For these reasons, resonance-trapped BICs based devices manifest practical advantages compared to symmetry-protected BICs devices, as they are more robust in terms of fabrication tolerances and their high Q-factor over a broader region of k-space renders them less prone to performance deterioration due to the dispersion relation of real finite lattices [106]. A promising example of such resonance-trapped BIC lasers is represented by optically pumped cylindrical nanoarrays in AlInGaAsP MQWs [107], which exhibits single-mode lasing regime over a wide region of k-space (demonstrated by the variability of the fabricated devices) and low lasing threshold in the sub-mW range, encouraging further research on topological BIC phenomena for alternative sensors and low-power sources (Fig. 16).

12. Topological photonic crystal lasers

Recent advances in topological photonics, derived from the bosonic analogue of topological insulators [108], whose properties and geometries manifest themselves in the generation of edge-states exhibiting lossless current transport (even in the presence of disorder) despite the insulating behaviour of the material in the bulk, have considerable potential for the development new compact semiconductor laser devices. Topological photonic behaviour is expressed by the presence of (topological) edge modes that protects light propagation against disorder. For this phenomenon to occur, breaking of time-reversal symmetry (TRS) is most often required [109] and various TRS-breaking devices have been postulated and later demonstrated, from gyro-optics materials in a magnetic field [110], to polarization controlled aperiodic resonators [111–113], bianisotropic metamaterials [114] and Photonic Crystals [115,116]. The presence of these topologically protected photonic edge modes, and their great potential for the development of disorder-immune lossless optical waveguides, has stimulated a research effort towards the implementation of active media onto topological material, aiming at the realization of a new class of efficient semiconductor lasers [46].

In the view of potential applications of topological lasers in dense photonic integrated circuits, which require considerably small device footprints, low power consumption and typically high-speed of operation, microcavity-based configurations [117–119] are attracting the most attention in silicon photonics. 1D and 2D PhC cavity-based topological lasers are particularly interesting, due to the already mentioned capability of PhCs to enhance the light-matter interaction, leading to improvements in the lasing performances such as high energy efficiency due to the high Q/V ratios and reduced lasing thresholds due to improvements in the spontaneous emission coupling factor. Indeed, the presence of topological edge states at the interface between different topological materials and the ability to deterministically predict them through the bulk-edge correspondence has proven a powerful tool for the tailoring of optical modes in PhC resonators and PhC cavity-based topological lasers have recently been demonstrated, such as defect-based PhC L3 cavity arrays supporting lasing at the 0D topological edge-states [120], optically pumped continuum PhC-based topological lasers operating at the Aubry-André-Harper 1D edge-states [121] and single-mode topological lasers based on 1D PhC nanobeams with distinct Zak phases with 0D topological edge-states exhibiting with Q-factors $\sim 10^5$ and high spontaneous emission coupling factor ten times larger than conventional semiconductor lasers (ß ~ 0.03) [122] (Fig. 17).

Optical Materials EXPRESS

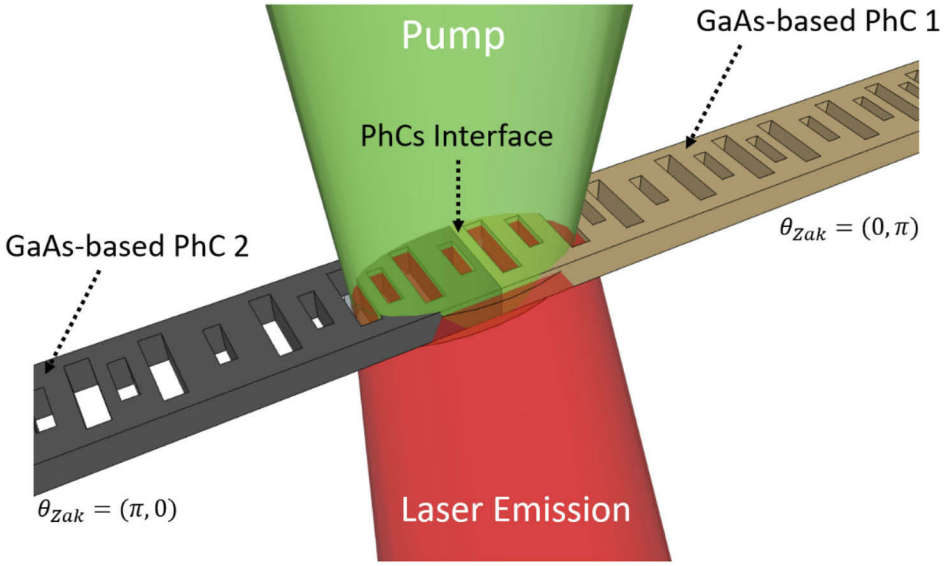

Fig. 17. Schematics of an optically pumped topological laser device supporting lasing at the edge modes generated by the presence of an interface between two different 1D PhC cavities, as in the device configuration of [122].

The topologically protected properties of all these topological laser prototype could prove critical for the development of advanced lasing operations such as: unidirectional light emission, back-scattering noise immunity, electron-spin-manipulation and lasing light steering [123].

Optical Materials EXPRESS

13. μTransfer-printing of semiconductor lasers on SOI PICs: a potential integration scheme for HECLs

Silicon based resonant modulators. One of the most efficient and flexible approaches to insert the light emitted by InP components into the SOI waveguides is edge-coupling, which provides broad band, polarization-agnostic low coupling losses of less than 1 dB [124] and avoids the need to create tapers on the InP, reducing its footprint and cost. Various integration techniques have been demonstrated that use die/wafer bonding [22,125–130], which also unlocks HECL configurations [71]. However, the die/wafer bonding approach is associated with a great waste of expensive material (i.e., InP), hence high cost. This issue can be completely removed by means of using Micro Transfer Printing (μTP), which offers high-throughput, parallel and scalable transfer of devices or dies of material to the desired locations on any platform, with sub-micron accuracy and no waste of III-V material associated. As a consequence, integration on silicon photonics of InP-based Fabry-Perot and DFB lasers and LEDs through μTP have been recently demonstrated [131–134].

HECLs are compatible with an advanced type of μTP integration approach exploiting evaporated metals as thermal vias, which also offers nanometric control on vertical alignment between the III-V gain and the passive chip, often required to achieve good laser performances.

In [62], the first heterogeneous integration of O-band Fabry-Perot InP lasers into SOI recesses by μTP and their edge-coupling to SU8 polymer waveguides was reported and it is expanded upon in this section. The approach allows a very accurate engineering of the alignment between InP lasers and polymer waveguides, also introducing the use of an intermediate metal layer deposited at the bottom of the oxide trench to calibrate the alignment along the vertical axis with sub-micron precision and sink the heat produced by the InP laser to the Si substrate. The configuration provides reduced thermal impedance compared to devices integrated on the SOI layer [31]. Moreover, a different geometry of the thermal via is simulated here and shows how the thermal sink could be further improved.

The etched-facet InP O-band lasers were undercut and released from their substrate and heterogeneously integrated by μTP to trenches etched on a SOI wafer, pre-patterned with Si waveguides to be incorporated in the polymer waveguides for mode conversion. The process involves shearing the laser coupon to the oxide sidewalls while in light contact with the bottom of the trench, completing the bond with the target when aligned. A 170 nm thick metal layer was pre-deposited on the bottom of the trench by means of e-beam evaporation to allow a very fine tuning of the alignment of the lasers with the waveguides along the vertical axis and heat dissipation from the laser to the Si substrate. The lateral alignment of the emitting facet of the lasers was ensured by μTP accuracies, improved by matching the devices to one of the trenches sidewalls. A very high adhesion yield of the printed devices (>90%) was achieved thanks to the use of a <3 nm thin vapour coated HDMS layer. After the printing, straight SU8 polymer waveguides were defined on top of the SiO_2 and Si tapered waveguides, in edge-coupling configuration with the laser (Fig. 18), achieving sub-micrometre lateral misalignment.

550 μm long and 60-80 μm wide micro-transfer-printable coupons constituted the laser, fabricated on an InP wafer as dense arrays. The two dry etched facets on the InP defined the Fabry-Perot cavity, then passivated by an optically neutral layer of SiO_2, while a metal coating was deposited on the back facet to improve reflectivity. A ridge etched on the active region provided the lateral confinement of the light required for single mode propagation. The laser coupons were then released from their native substrate by selective wet etching of a sacrificial layer. The suspended structures were then transfer-printed epitaxial-side-up to prefabricated recesses on the SOI. E-beam lithography (EBL) and a series of dry etches were used to define tapered waveguides on the 220 nm thick Si and to open the trenches in the oxide to accommodate the coupons on the SOI. A metal layer (Ti:Au) was evaporated with nm-scale accuracy, crucial

Optical Materials EXPRESS

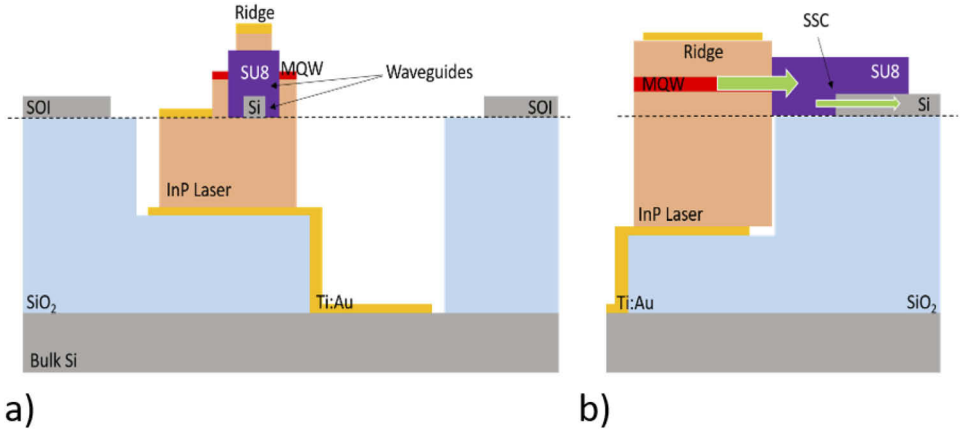

Fig. 18. Schematics of the Transfer-Printed laser coupon on the SOI, a) is the cross-section view and b) represents the side view of the integrated laser on the SiP chip

for the vertical alignment between the lasers and polymer waveguides. SU8 polymer waveguides were defined by means of EBL for the edge-coupling with the ridges of the lasers.

Electrical and optical characterization of the InP laser was performed before and after μTP to the recess and after edge-coupling to the SU8 waveguide. The LI characteristics of the lasers showed an unaffected threshold current of I_{th} ~17 mA before and after μTP to the SOI. An increase of the threshold I_{th} to ~23 mA after coupling the light to the SU8 waveguide was observed, related to the reduced reflectivity on the front mirror from R ~32% (in air) to R ~15.5% (SU8). The thermal impedances of the lasers were measured in the range of ZEXP ~116 K/W.

The improved longitudinal alignment and lack of rotation achieved by matching the laser coupons to the sidewalls of the recesses and the nanometre control on the vertical alignment introduced by the evaporated Ti:Au thermal vias shown in [62] can reliably address the gain-PIC alignment requirements of HECLs, unlocking the possibility to further reduce the costs related to HECL integration.

14. Conclusions

In this review, different configurations of semiconductor PhC-based lasers have been discussed. These laser architectures exploit the many advantages of Photonic Crystal cavities, such as small footprint, strong confinement of light in tight spaces (~λ^3), wavelength selectivity, beam shaping, and enhanced non-linear dynamics. This has enabled high brightness lasing (e.g., in PCSELs and BIC Lasers) for LIDAR and imaging applications; low-switching energy direct light modulation (e.g., in LEAP lasers) for telecom applications; athermal lasing operation and design/employment versatility (e.g. in HECLs) for datacom, optical sensing and biomedical applications. Looking to the future, the ability to independently optimize the gain and passive chips used by the HECL configuration will support improved optical, thermal and mechanical performance. Crucially, HECLs have also been shown to be compatible with novel, highly scalable and low-cost integration schemes, such as μTransfer Printing, offering a future economy of scale in the production of these devices. Moreover, recent research interest towards novel laser prototypes operating in topologically protected regimes points towards a future class of compact semiconductor lasers with advanced functionalities, from high angle beam steering to unidirectional backscattering unsusceptible lasing in harsh and tight environments.

Funding. Engineering and Physical Sciences Research Council (EPRC); Horizon 2020 Framework Programme

Optical Materials EXPRESS

(780240 REDFICH, COSMIC 688516, ERC337508, H2020-ICT27-2015, LEIT ICT); Science Foundation Ireland (16/ERCS/3838, 18/TIDA/6128, SFI12/RC/2276).

Acknowledgements. The authors gratefully acknowledge Science Foundation Ireland (SFI) (16/ERCS/3838, SFI12/RC/2276); (EP/L017008/1, EP/L505079/1); H2020 LEIT Information and Communication Technologies (ICT); COSMICC 688516; H2020-ICT27-2015); Research Council (EPSRC); H2020 European Research Council (ERC) (337508), SFI 18/TIDA/6128, and H2020 780240 (REDFINCH)

Disclosures. The authors declare no conflicts of interest.

References

1. J. Hecht, "Integrated photonics: photonic integration may boost computing performance", Tech. rep., pp. 1–5 (2011).
2. C. Gunn, "CMOS Photonics for High-Speed Interconnects," IEEE Computer Society **26**(2), 58–66 (2006).
3. C. F. Lam, H. Liu, B. Koley, X. Zhao, V. Kamalov, and V. Gill, "Fiber optic communication technologies: what's needed for datacenter network operations," IEEE Commun. Mag. **48**(7), 32–39 (2010).
4. A. Benner, "Optical interconnect opportunities in supercomputers and high-end computing," in *Optical Fiber Communication Conference (OFC)*, 2012 OSA Technical Digest Series, paper OTu2B (2012).
5. D. A. B. Miller, "Optical interconnects to silicon," IEEE J. Select. Topics Quantum Electron. **6**(6), 1312–1317 (2000).
6. Y. A. Vlsaov, "Silicon photonics for next generation computing systems," in *Proceedings of European Conference on Optical Communications*, paper SC2, (2008).
7. D. A. B. Miller, "Device requirements for optical interconnects to silicon chips," Proc. IEEE **97**(7), 1166–1185 (2009).
8. K. Adachi, K. Shinoda, T. Kitatani, T. Fukamachi, Y. Matsuoka, T. Sugawara, and S. Tsuji, "25-Gb/s multichannel 1.3-μm surface-emitting lens-integrated DFB laser arrays," J. Lightwave Technol. **29**(19), 2899–2905 (2011).
9. S. Matsuo, T. Fujii, K. Hasebe, K. Takeda, T. Sato, and T. Kakitsuka, "Directly modulated buried heterostructure DFB laser on SiO_2/Si substrate fabricated by regrowth of InP using bonded active layer," Opt. Express **22**(10), 12139–12147 (2014).
10. W. Kobayashi, T. Ito, T. Yamanaka, T. Fujisawa, Y. Shibata, T. Kurosaki, M. Kohtoku, T. Tadokoro, and H. Sanjoh, "50-Gb/s direct modulation of a 1.3-μm InGaAlAs-based DFB laser with a ridge waveguide structure," IEEE J. Sel. Top. Quantum Electron. **19**(4), 1500908 (2013).
11. S. Imai, K. Takaki, S. Kamiya, H. Shimizu, J. Yoshida, Y. Kawakita, T. Takagi, K. Hiraiwa, H. Shimizu, T. Suzuki, N. Iwai, T. Ishikawa, N. Tsukiji, and A. Kasukawa, "Recorded low power dissipation in highly reliable 1060-nm VCSELs for "Green" optical interconnection," IEEE J. Sel. Top. Quantum Electron. **17**(6), 1614–1620 (2011).
12. W. Hofmann, P. Moser, and D. Bimberg, "Energy-efficient VCSELs for interconnects," IEEE Photonics J. **4**(2), 652–656 (2012).
13. S. Noda, M. Yokoyama, M. Imada, A. Chutinan, and M. Mochizuki, "Polarization mode control of two-dimensional photonic crystal laser by unit cell structure design," Science **293**(5532), 1123–1125 (2001).
14. E. Miyai, K. Sakai, T. Okano, W. Kunishi, D. Ohnishi, and S. Noda, "Lasers producing tailored beams," Nature **441**(7096), 946 (2006).
15. S. Iwahashi, Y. Kurosaka, K. Sakai, K. Kitamura, N. Takayama, and S. Noda, "High-order vector beams produced by photonic-crystal lasers," Opt. Express **19**(13), 11963–11968 (2011).
16. S. Matsuo, A. Shinya, T. Kakitsuka, K. Nozaki, T. Segawa, T. Sato, Y. Kawaguchi, and M. Notomi, "High-speed ultracompact buried heterostructure photonic-crystal laser with 13 fJ of energy consumed per bit transmitted," Nat. Photonics **4**(9), 648–654 (2010).
17. J. E. Bowers, D. Huang, D. Jung, J. Norman, M. A. Tran, Y. Wan, W. Xie, and Z. Zhang, "Realities and challenges of III-V/Si integration technologies," in *Optical Fiber Communication Conference (OFC) 2019*, OSA Technical Digest, (2019).
18. J. M. Ramirez, H. Elfaiki, T. Verolet, C. Besancon, A. Gallet, D. Néel, K. Hassan, S. Olivier, C. Jany, S. Malhouitre, K. Gradkowski, P. E. Morrissey, P. O'Brien, C. Caillaud, N. Vaissière, J. Decobert, S. Lei, R. Enright, A. Shen, and M. Achouche, "III-V-on-Silicon Integration: From Hybrid Devices to Heterogeneous Photonic Integrated Circuits," IEEE J. Sel. Top. Quantum Electron. **26**(2), 1–13 (2020).
19. F. E. Doany, R. Budd, L. Schares, T. Huynh, M. Wood, D. Kuchta, N. Dupuis, C. Schow, B. Lee, M. Moehrle, A. Sigmund, W. Rehbein, T. Y. Liow, L. W. Luo, and G. Q. Lo, "A four-channel silicon photonic carrier with flip-chip integrated semiconductor optical amplifier (SOA) array providing >10-dB gain," in *IEEE 66th Electronic Components and Technology Conference (ECTC)*, 1061–1068 (2016).
20. G.-H. Duan, C. Jany, A. Le Liepvre, A. Accard, M. Lamponi, D. Make, P. Kaspar, G. Levaufre, N. Girard, F. Lelarge, J.-M. Fedeli, S. Messaoudene, D. Bordel, and S. Olivier, "Hybrid III-V on silicon lasers for photonic integrated circuits on silicon," IEEE J. Sel. Top. Quantum Electron. **20**(4), 158–170 (2014).
21. K. Tanabe, K. Watanabe, and Y. Arakawa, "III-V/Si hybrid photonic devices by direct fusion bonding," Sci. Rep. **2**(1), 349 (2012).
22. A. W. Fang, H. Park, O. Cohen, R. Jones, M. J. Paniccia, and J. E. Bowers, "Electrically pumped hybrid AlGaInAs-silicon evanescent laser," Opt. Express **14**(20), 9203–9210 (2006).

Optical Materials EXPRESS

23. T. Hong, G.-Z. Ran, T. Chen, J.-Q. Pan, W.-X. Chen, Y. Wang, Y.-B. Cheng, S. Liang, L.-J. Zhao, L.-Q. Yin, J.-H. Zhang, W. Wang, and G.-G. Qin, "A selective-area metal bonding InGaAsP–Si laser," IEEE Photonics Technol. Lett. **22**(15), 1141–1143 (2010).
24. M. J. R. Heck, J. F. Bauters, M. L. Davenport, J. K. Doylend, S. Jain, G. Kurczveil, S. Srinivasan, Y. Tang, and J. E. Bowers, "Hybrid silicon photonic integrated circuit technology," IEEE J. Sel. Top. Quantum Electron. **19**(4), 6100117 (2013).
25. J. Van Campenhout, P. Rojo-Romeo, D. Van Thourhout, C. Seassal, P. Regreny, L. Di Cioccio, J.-M. Fedeli, and R. Baets, "Thermal characterization of electrically injected thin-film InGaAsP microdisk lasers on Si," J. Lightwave Technol. **25**(6), 1543–1548 (2007).
26. Y. de Koninck, F. Raineri, A. Bazin, R. Raj, G. Roelkens, and R. Baets, "Experimental demonstration of a hybrid III–V-on-silicon microlaser based on resonant grating cavity mirrors," Opt. Lett. **38**(14), 2496–2498 (2013).
27. G. Crosnier, D. Sanchez, S. Bouchoule, P. Monnier, G. Beaudoin, I. Sagnes, R. Raj, and F. Raineri, "Hybrid indium phosphide-on-silicon nanolaser diode," Nat. Photonics **11**(5), 297–300 (2017).
28. Z. Zhou, B. Yin, and J. Michel, "On-chip light sources for silicon photonics," Light: Sci. Appl. **4**(11), e358 (2015).
29. J.-H. Lee, J. Bovington, I. Shubin, Y. Luo, J. Yao, S. Lin, J. E. Cunningham, K. Raj, A. V. Krishnamoorthy, and X. Zheng, "Demonstration of 12.2% wall plug efficiency in uncooled single mode external-cavity tunable Si/III-V hybrid laser," Opt. Express **23**(9), 12079–12088 (2015).
30. G. D. Maxwell, R. Kashyap, G. Sherlock, J. V. Collins, and B. J. Ainslie, "Demonstration of a semiconductor external cavity laser using a UV written grating in a planar silica waveguide," Electron. Lett. **30**(18), 1486–1487 (1994).
31. A. J. Zilkie, P. Seddighian, B. J. Bijlani, W. Qian, D. C. Lee, S. Fathololoumi, J. Fong, R. Shafiiha, D. Feng, B. J. Luff, X. Zheng, J. E. Cunningham, A. V. Krishnamoorthy, and M. Asghari, "Power-efficient III-V/silicon external cavity DBR lasers," Opt. Express **20**(21), 23456–23462 (2012).
32. J.-U. Shin, S. H. Oh, Y.-J. Park, S.-H. Park, Y.-T. Han, H. Sung, and K. R. Oh, "External cavity lasers composed of higher order gratings and SLDs integrated on PLC platform," ETRI J. **29**(4), 452–456 (2007).
33. A. W. Fang, B. R. Koch, R. Jones, E. Lively, D. Liang, Y.-H. Kuo, and J. E. Bowers, "A distributed Bragg reflector silicon evanescent laser," IEEE Photonics Tech. Lett. **20**(20), 1667–1669 (2008).
34. J. A. Davis, M. S. Kim, A. El Amili, D. C. Trotter, A. L. Starbuck, C. Dallo, A. T. Pomerene, C. T. DeRose, A. L. Lentine, and Y. Fainman, "III/V silicon hybrid laser based on a resonant Bragg structure," Appl. Opt. **59**(13), 4158–4164 (2020).
35. S. Li, D. Zhang, J. Zhao, Q. Yang, X. Xiao, S. Hu, L. Wang, M. Li, X. Tang, Y. Qiu, M. Luo, and S. Yu, "Silicon micro-ring tunable laser for coherent optical communication," Opt. Express **24**(6), 6341–6349 (2016).
36. T. Chu, N. Fujioka, and M. Ishizaka, "Compact, lower-power-consumption wavelength tunable laser fabricated with silicon photonic wire waveguide micro-ring resonators," Opt. Express **17**(16), 14063–14068 (2009).
37. Y. Zhang, S. Yang, H. Guan, A. E.-J. Lim, G.-Q. Lo, P. Magill, T. Baehr-Jones, and M. Hochberg, "Sagnac loop mirror and micro-ring based laser cavity for silicon-on-insulator," Opt. Express **22**(15), 17872–17879 (2014).
38. K. Debnath, L. O'Faolain, F. Y. Gardes, A. G. Steffan, G. T. Reed, and T. F. Krauss, "Cascaded modulator architecture for WDM applications," Opt. Express **20**(25), 27420–27428 (2012).
39. A. A. Liles, K. Debnath, and L. O'Faolain, "Lithographic wavelength control of an external cavity laser with a silicon photonic crystal cavity-based resonant reflector," Opt. Lett. **41**(5), 894–897 (2016).
40. S. M. Butler, A. P. Bakoz, P. K. J. Singaravelu, A. A. Liles, B. O'Shaughnessy, E. A. Viktorov, L. O'Faolain, and S. P. Hegarty, "Frequency modulated hybrid photonic crystal laser by thermal tuning," Opt. Express **27**(8), 11312–11322 (2019).
41. S. Iadanza, G. C. R. Devarapu, A. A. Liles, R. Sheehan, and L. O'Faoláin, "Hybrid external cavity laser with an amorphous silicon-based photonic crystal cavity mirror," Appl. Sci. **10**(1), 240 (2020).
42. M. Meier, A. Mekis, A. Dodabalapur, A. Timko, R. E. Slusher, J. D. Joannopoulos, and O. Nalamasu, "Laser action from two-dimensional distributed feedback in photonic crystals," Appl. Phys. Lett. **74**(1), 7–9 (1999).
43. H. Matsubara, S. Yoshimoto, H. Saito, Y. Jianglin, Y. Tanaka, and S. Noda, "GaN photonic-crystal surface-emitting laser at blue-violet wavelengths," Science **319**(5862), 445–447 (2008).
44. K. Hirose, Y. Liang, Y. Kurosaka, A. Watanabe, T. Sugiyama, and S. Noda, "Watt-class high-power, high-beam-quality photonic-crystal lasers," Nat. Photonics **8**(5), 406–411 (2014).
45. A. A. Yanik, A. E. Cetin, M. Huang, A. Artar, S. H. Mousavi, A. Khanikaev, J. H. Connor, G. Shvets, and H. Altug, "Seeing protein monolayers with naked eye through plasmonic Fano resonances," Proc. Natl. Acad. Sci. U. S. A. **108**(29), 11784–11789 (2011).
46. J. M. Foley, S. M. Young, and J. D. Phillips, "Symmetry-protected mode coupling near normal incidence for narrow-band transmission filtering in a dielectric grating," Phys. Rev. B **89**(16), 165111 (2014).
47. Y. Ota, K. Takata, T. Ozawa, A. Amo, Z. Jia, B. Kante, M. Notomi, Y. Arakawa, and S. Iwamoto, "Active topological photonics"," Nanophotonics **9**(3), 547–567 (2020).
48. K. Sakai, E. Miyai, and S. Noda, "Two-dimensional coupled wave theory for square-lattice photonic-crystal lasers with TM-polarization," Opt. Express **15**(7), 3981–3990 (2007).
49. H. Y. Ryu, S. H. Kwon, Y. J. Lee, and Y. H. Lee, "Very-low-threshold photonic band-edge lasers from free-standing triangular photonic crystal slabs," Appl. Phys. Lett. **80**(19), 3476–3478 (2002).

Optical Materials EXPRESS

50. M. Imada, S. Noda, A. Chutinan, and T. Tokuda, "Coherent two-dimensional lasing action in surface-emitting laser with triangular-lattice photonic crystal structure," Appl. Phys. Lett. **75**(3), 316–318 (1999).
51. H.-Y. Lu, S.-C. Tian, C.-Z. Tong, L.-J. Wang, J.-M. Rong, C.-Y. Liu, H. Wang, S.-L. Shu, and L.-J. Wang, "Extracting more light for vertical emission: high power continuous wave operation of 1.3-μm quantum-dot photonic-crystal surface-emitting laser based on a flat band," Light: Sci. Appl. **8**(1), 108 (2019).
52. X. L. Yang, L. Z. Cai, and Q. Liu, "Theoretical bandgap modeling of two-dimensional triangular photonic crystals formed by interference technique of three noncoplanar beams," Opt. Express **11**(9), 1050–1055 (2003).
53. T. Sakaguchi, "Fabrication of photonic-crystal lasers by MOCVD regrowth technique (II)," presented at *71st Japanese Society Appl. Physics, Autumn Meeting*, Nagasaki, Japan, Sep. 14–17, 2010, Paper 16p-J-10.
54. S. Noda, K. Kitamura, T. Okino, D. Yasuda, and Y. Tanaka, "Photonic-crystal surface-emitting lasers: review and introduction of modulated-photonic crystals," IEEE J. Sel. Top. Quantum Electron. **23**(6), 1–7 (2017).
55. K. Takeda, T. Sato, A. Shinya, K. Nozaki, W. Kobayashi, H. Taniyama, M. Notomi, K. Hasebe, T. Kakitsuka, and S. Matsuo, "Few-fJ/bit data transmissions using directly modulated lambda-scale embedded active region photonic-crystal lasers," Nat. Photonics **7**(7), 569–575 (2013).
56. K. Takeda, T. Sato, T. Fujii, E. Kuramochi, M. Notomi, K. Hasebe, T. Kakitsuka, and S. Matsuo, "Heterogeneously integrated photonic-crystal lasers on silicon for on/off chip optical interconnects," Opt. Express **23**(2), 702–708 (2015).
57. A. Shinya, T. Sato, K. Takeda, K. Nozaki, E. Kuramochi, T. Kakitsuka, H. Taniyama, T. Fujii, S. Matsuo, and M. Notomi, "Single-mode lasing of Lambda-scale Embedded Active-region Photonic-crystal (LEAP) laser with in-line coupled waveguide," *2013 IEEE Photonics Conference*, 448–449 (2013).
58. S. Matsuo and K. Takeda, "λ-Scale Embedded Active Region Photonic Crystal (LEAP) Lasers for Optical Interconnects," Photonics **6**(3), 82 (2019).
59. S. Matsuo, A. Shinya, C.-H. Chen, K. Nozaki, T. Sato, Y. Kawaguchi, H. Taniyama, and M. Notomi, "20-Gbit/s directly modulated photonic crystal nanocavity laser with ultra-low power consumption," Opt. Express **19**(3), 2242–2250 (2011).
60. Y. Urino, T. Usuki, J. Fujikata, M. Ishizaka, K. Yamada, T. Horikawa, T. Nakamura, and Y. Arakawa, "High-density and wide-bandwidth optical interconnects with silicon optical interposers [Invited]," Photonics Res. **2**(3), A1–A7 (2014).
61. S. Tanaka, S.-H. Jeong, S. Sekiguchi, T. Kurahashi, Y. Tanaka, and K. Morito, "High-output-power, single-wavelength silicon hybrid laser using precise flip-chip bonding technology," Opt. Express **20**(27), 28057–28069 (2012).
62. R. Loi, S. Iadanza, B. Roycroft, J. O'Callaghan, L. Liu, K. Thomas, A. Gocalinska, E. Pelucchi, A. Farrell, S. Kelleher, R. F. Gul, A. J. Trinidade, D. Gomez, L. O'Faolain, and B. Corbett, "Edge-Coupling of O-Band InP Etched-Facet Lasers to Polymer Waveguides on SOI by Micro-Transfer-Printing," IEEE J. Quantum Electron. **56**(1), 1–8 (2020).
63. B. Haq, J. R. Vaskasi, J. Zhang, A. Gocalinska, E. Pelucchi, B. Corbett, and G. Roelkens, "Micro-transfer-printed III-V-on-silicon C-band distributed feedback lasers," Opt. Express **28**(22), 32793 (2020).
64. Y. Gideon, T. Nguyen, J. Heanue, and B. Pezeshki, "Efficient compact tun-able laser for access networks using silicon ring resonators," *Optical Fiber Communication Conference and Exposition (OFC) and National Fiber Optic Engineers Conference (OFC/NFOEC)* 1–3 (2012).
65. J. Komma, C. Schwarz, G. Hofmann, D. Heinert, and R. Nawrodt, "Thermo-optic coefficient of silicon at 1550 nm and cryogenic temperatures," Appl. Phys. Lett. **101**(4), 041905 (2012).
66. Optomark, "DWDM multiplexers," http://www.optomark.eu/products/cwdm-dwdm/dwdm-multiplexers.html
67. FibeReality, "100G transceivers below $3/Gig by 2017?", http://fibereality.com/blog/100g-transceivers-below-3gig-by-2017/
68. C. Wang, X. Li, H. Jin, H. Yu, J. Yang, and X. Jiang, "Silicon reflectors for external cavity lasers based on ring resonators," Opt. Commun. **383**, 453–459 (2017).
69. Y. Fan, J. P. Epping, R. M. Oldenbeuving, C. G. H. Roeloffzen, M. Hoekman, R. Dekker, R. G. Heideman, P. J. M. van der Slot, and K.-J. Boller, "Optically integrated In-Si3N4 hybrid laser," IEEE Photonics J. **8**(6), 1–11 (2016).
70. A. Arbabi and L. L. Goddard, "Measurements of the refractive indices and thermo-optic coefficients of Si3N4 and SiOx using microring resonances," Opt. Lett. **38**(19), 3878–3881 (2013).
71. S. Iadanza, A. P. Bakoz, P. K. J. Singaravelu, D. Panettieri, S. A. Schulz, G. C. R. Devarapu, S. Guerber, C. Baudot, F. Boeuf, S. Hegarty, and L. O'Faolain, "Thermally stable hybrid cavity laser based on silicon nitride gratings," Appl. Opt. **57**(22), E218–E223 (2018).
72. E. Murphy, C. Michie, H. White, W. Johnstone, A. E. Kelly, and I. Andonovic, "High temperature wavelength division network for avionic applications," J. Lightwave Technol. **31**(18), 3006–3013 (2013).
73. S. Iadanza, M. Clementi, C. Hu, S. A. Schulz, D. Gerace, M. Galli, and L. O'Faolain, "Model of thermo-optic nonlinear dynamics of photonic crystal cavities," Phys. Rev. B **102**(24), 245404 (2020).
74. A. Bakoz, A. A. Liles, A. A. Gonzalez-Fernandez, T. Habruseva, C. Hu, E. A. Viktorov, S. P. Hegarty, and L. O'Faolain, "Wavelength stability in a hybrid photonic crystal laser through controlled nonlinear absorptive heating in the reflector," Light: Sci. Appl. **7**(1), 39 (2018).
75. K. Debnath, K. Welna, M. Ferrera, K. Deasy, D. G. Lidzey, and L. O'Faolain, "Highly efficient optical filter based on vertically coupled photonic crystal cavity and bus waveguide," Opt. Lett. **38**(2), 154–156 (2013).

Optical Materials EXPRESS

76. S.-W. Jeon, J.-K. Han, B.-S. Song, and S. Noda, "Glass-embedded two-dimensional silicon photonic crystal devices with a broad bandwidth waveguide and a high quality nanocavity," Opt. Express **18**(18), 19361–19366 (2010).
77. T. P. White, L. O'Faolain, J. Li, L. C. Andreani, and T. F. Krauss, "Silica-embedded silicon photonic crystal waveguides," Opt. Express **16**(21), 17076–17081 (2008).
78. B.-S. Song, S.-W. Jeon, and S. Noda, "Symmetrically glass-clad photonic crystal nanocavities with ultrahigh quality factors," Opt. Lett. **36**(1), 91–93 (2011).
79. K. Welna, S. L. Portalupi, M. Galli, L. O'Faolain, and T. F. Krauss, "Novel dispersion adapted photonic crystal cavity with improved disorder stability," IEEE J. Quantum Electron. **48**(9), 1177–1183 (2012).
80. K. Welna, K. Debnath, T. F. Kraus, and L. O'Faolain, "High-Q photonic crystal cavities realised using deep ultraviolet lithography," Electron. Lett. **51**(16), 1277–1279 (2015).
81. F. Y. Gardes, A. Brimont, P. Sanchis, G. Rasigade, D. Marris-Morini, L. O'Faolain, F. Dong, J. M. Fedeli, P. Dumon, L. Vivien, T. F. Krauss, G. T. Reed, and J. Marti, "High-speed modulation of a compact silicon ring resonator based on a reverse-biased pn diode," Opt. Express **17**(24), 21986–21991 (2009).
82. Q. Xu, S. Manipatruni, B. Schmidt, J. Shakya, and M. Lipson, "12.5 Gbit/s carrier-injection-based silicon micro-ring silicon modulators," Opt. Express **15**(2), 430–436 (2007).
83. P. Dong, W. Qian, H. Liang, R. Shafiiha, N.-N. Feng, D. Feng, X. Zheng, A. V. Krishnamoorthy, and M. Asghari, "Low power and compact reconfigurable multiplexing devices based on silicon microring resonators," Opt. Express **18**(10), 9852–9858 (2010).
84. G. Li, A. V. Krishnamoorthy, I. Shubin, J. Yao, Y. Luo, H. Thacker, X. Zheng, K. Raj, and J. E. Cunningham, "Ring resonator modulators in silicon for interchip photonic links," IEEE J. Sel. Top. Quantum Electron. **19**(6), 95–113 (2013).
85. P. Dong, W. Qian, H. Liang, R. Shafiiha, D. Feng, G. Li, J. E. Cunningham, A. V. Krishnamoorthy, and M. Asghari, "Thermally tunable silicon racetrack resonators with ultralow tuning power," Opt. Express **18**(19), 20298–20304 (2010).
86. J.-B. You, M. Park, J.-W. Park, and G. Kim, "12.5 Gbps optical modulation of silicon racetrack resonator based on carrier-depletion in asymmetric p-n diode," Opt. Express **16**(22), 18340–18344 (2008).
87. E. Timurdogan, C. M. Sorace-Agaskar, J. Sun, E. S. Hosseini, A. Biberman, and M. R. Watts, "An ultralow power athermal silicon modulator," Nat. Commun. **5**(1), 4008 (2014).
88. M. R. Watts, W. A. Zortman, D. C. Trotter, R. W. Young, and A. L. Lentine, "Vertical junction silicon microdisk modulators and switches," Opt. Express **19**(22), 21989–22003 (2011).
89. T. Tanabe, K. Nishiguchi, E. Kuramochi, and M. Notomi, "Low power and fast electro-optic silicon modulator with lateral p-i-n embedded photonic crystal nanocavity," Opt. Express **17**(25), 22505 (2009).
90. S. M. Butler, P. K. J. Singaravelu, L. O'Faolain, and S. P. Hegarty, "Long cavity photonic crystal laser in FDML operation using an akinetic reflective filter," Opt. Express **28**(26), 38813–38821 (2020).
91. R. Huber, M. Wojtkowski, and J. G. Fujimoto, "Fourier Domain Mode Locking (FDML): A new laser operating regime and applications for optical coherence tomography," Opt. Express **14**(8), 3225–3237 (2006).
92. M. A. Choma, K. Hsu, and J. A. Izatt, "Swept source optical coherence tomography using an all-fiber 1300-nm ring laser source," J. Biomed. Opt. **10**(4), 044009 (2005).
93. C. Jun, M. Villiger, W.-Y. Oh, and B. E. Bouma, "All-fiber wavelength swept ring laser based on Fabry-Perot filter for optical frequency domain imaging," Opt. Express **22**(21), 25805–25816 (2014).
94. R. Huber, M. Wojtkowski, K. Taira, and J. G. Fujimoto, "Amplified, frequency swept lasers for frequency domain reflectometry and OCT imaging: design and scaling principles," Opt. Express **13**(9), 3513–3528 (2005).
95. A. M. Yacomotti, L. Furfaro, X. Hachair, F. Pedaci, M. Giudici, J. Tredicce, J. Javaloyes, S. Balle, E. A. Viktorov, and P. Mandel, "Dynamics of multimode semiconductor lasers," Phys. Rev. A **69**(5), 053816 (2004).
96. T. Butler, S. Slepneva, B. O'Shaughnessy, B. Kelleher, D. Goulding, S. P. Hegarty, H.-C. Lyu, K. Karnowski, M. Wojtkowski, and G. Huyet, "Single shot, time-resolved measurement of the coherence properties of OCT swept source lasers," Opt. Lett. **40**(10), 2277–2280 (2015).
97. J. Von Neumann and E. P. Wigner, "Über merkwürdige diskrete Eigenwerte," Z. Phys. **30**, 465–467 (1929).
98. C. Hsu, B. Zhen, A. D. Stone, J. D. Joannopoulos, and M. Soliacic, "Bound states in the continuum," Nat. Rev. Mater. **1**(9), 16048 (2016).
99. H. Friedrich and D. Wintgen, "Interfering resonances and bound states in the continuum," Phys. Rev. A **32**(6), 3231–3242 (1985).
100. X. Gao, C. Hsu, B. Zhen, X. Lin, J. D. Joannopoulos, M. Soliacic, and H. Chen, "Formation mechanism of guided resonances and bound states in the continuum in photonic crystal slabs," Sci. Rep. **6**(1), 31908 (2016).
101. C. H. Henry, R. F. Kazarinov, R. A. Logan, and R. Yen, "Observation of destructive interference in the radiation loss of second-order distributed feedback lasers," IEEE J. Quantum Electron. **21**(2), 151–154 (1985).
102. B. Zhen, S. Chua, J. Lee, A. W. Rodriguez, X. Liang, S. G. Johnson, J. D. Joannopoulos, M. Soljačić, and O. Shapira, "Enabling Enhanced Emission and Low Threshold Lasing of Organic Molecules Using Special Fano Resonances of Macroscopic Photonic Crystals," in *CLEO: 2014*, OSA Technical Digest (2014).
103. K. Kitamura, K. Sakai, N. Takayama, M. Nishimoto, and S. Noda, "Focusing properties of vector vortex beams emitted by photonic-crystal lasers," Opt. Lett. **37**(12), 2421–2423 (2012).
104. Q. Zhan, "Cylindrical vector beams: from mathematical concepts to applications," Adv. Opt. Photonics **1**(1), 1–57 (2009).

Optical Materials EXPRESS

105. C. Hsu, B. Zhen, J. Lee, S.-L. Chua, S. G. Johnson, J. D. Joannopolous, and M. Soliacic, "Observation of trapped light within the radiation continuum," Nature **499**(7457), 188–191 (2013).
106. T. Xu, S. Yang, S. V. Nair, and H. E. Ruda, "Confined modes in finite-size photonic crystals," Phys. Rev. B **72**(4), 045126 (2005).
107. A. Kodigala, T. Lepetit, Q. Gu, B. Bahari, Y. Fainman, and B. Kanté, "Lasing action from photonic bound states in continuum," Nature **541**(7636), 196–199 (2017).
108. M. Segev and M. A. Bandres, "Topological photonics: Where do we go from here?" Nanophotonics **10**(1), 425–434 (2020).
109. F. D. M. Haldane and S. Raghu, "Possible realization of directional optical waveguides in photonic crystals with broken time-reversal symmetry," Phys. Rev. Lett. **100**(1), 013904 (2008).
110. Z. Wang, Y. D. Chong, J. D. Joannopoulos, and M. Soljačić, "Reflection-free one-way edge modes in a gyromagnetic photonic crystal," Phys. Rev. Lett. **100**(1), 013905 (2008).
111. M. Hafezi, E. A. Demler, M. D. Lukin, and J. M. Taylor, "Robust optical delay lines with topological protection," Nat. Phys. **7**(11), 907–912 (2011).
112. M. Hafezi, S. Mittal, J. Fan, A. Migdall, and J. M. Taylor, "Imaging topological edge states in silicon photonics," Nat. Photonics **7**(12), 1001–1005 (2013).
113. S. Mittal, J. Fan, S. Faez, A. Migdall, J. M. Taylor, and M. Hafezi, "Topologically robust transport of photons in a synthetic gauge field," Phys. Rev. Lett. **113**(8), 087403 (2014).
114. A. B. Khanikaev, S. Hossein Mousavi, W.-K. Tse, M. Kargarian, A. H. MacDonald, and G. Shvets, "Photonic topological insulators," Nat. Mater. **12**(3), 233–239 (2013).
115. R. O. Umucalılar and I. Carusotto, "Artificial gauge field for photons in coupled cavity arrays," Phys. Rev. A **84**(4), 043804 (2011).
116. L.-H. Wu and X. Hu, "Scheme for achieving a topological photonic crystal by using dielectric material," Phys. Rev. Lett. **114**(22), 223901 (2015).
117. M. Parto, S. Wittek, H. Hodaei, G. Harari, M. A. Bandres, J. Ren, M. C. Rechtsman, M. Segev, D. N. Christodoulides, and M. Khajavikhan, "Edge-mode lasing in 1D topological active arrays," Phys. Rev. Lett. **120**(11), 113901 (2018).
118. H. Zhao, P. Miao, M. H. Teimourpour, S. Malzard, R. El-Ganainy, H. Schomerus, and L. Feng, "Topological hybrid silicon microlasers," Nat. Commun. **9**(1), 981 (2018).
119. P. St-Jean, V. Goblot, E. Galopin E, A. Lemaître, T. Ozawa, L. Le Gratiet, I. Sagnes, J. Bloch, and A. Amo, "Lasing in topological edge states of a one-dimensional lattice," Nat. Photonics **11**(10), 651–656 (2017).
120. C. Han, M. Lee, S. Callard, C. Seassal, and H. Jeon, "Lasing at topological edge states in a photonic crystal L3 nanocavity dimer array," Light: Sci. Appl. **8**(1), 40 (2019).
121. L. Pilozzi and C. Conti, "Topological lasing in resonant photonic structures," Phys. Rev. B **93**(19), 195317 (2016).
122. Y. Ota, R. Katsumi, K. Watanabe, S. Iwamoto, and Y. Arakawa, "Topological photonic crystal nanocavity laser," Commun. Phys. **1**(1), 86 (2018).
123. H. Zhao, X. Qiao, T. Wu, B. Midya, S. Longhi, and L. Feng, "Non-Hermitian topological light steering," Science **365**(6458), 1163–1166 (2019).
124. L. Carroll, J.-S. Lee, C. Scarcella, K. Gradkowski, M. Duperron, H. Lu, Y. Zhao, C. Eason, P. Morrissey, M. Rensing, S. Collins, H. Y. Hwang, and P. O'Brien, "Photonic packaging: transforming silicon photonic integrated circuits into photonic devices," Appl. Sci. **6**(12), 426 (2016).
125. H. Guan, A. Novack, T. Galfsky, Y. Ma, S. Fathololoumi, A. Horth, T. N. Huynh, J. Roman, R. Shi, M. Caverley, Y. Liu, T. Baehr-Jones, K. Bergman, and M. Hochberg, "Widely-tunable, narrow-linewidth III-V/silicon hybrid external-cavity laser for coherent communication," Opt. Express **26**(7), 7920–7933 (2018).
126. S. Lin, S. S. Djordjevic, J. E. Cunningham, I. Shubin, Y. Luo, J. Yao, G. Li, H. Thacker, J.-H. Lee, K. Raj, X. Zheng, and A. V. Krishnamoorthy, "Vertical-coupled high-efficiency tunable III-V-CMOS SOI hybrid external-cavity laser," Opt. Express **21**(26), 32425–32431 (2013).
127. Y. Aoki, T. Kato, R. J. Mizuno, and K. Iga, "Micro-optical bench for alignment-free optical coupling," Appl. Opt. **38**(6), 963–965 (1999).
128. G. Roelkens, L. Liu, D. Liang, R. Jones, A. Fang, B. Koch, and J. E. Bowers, "III-V/silicon photonics for on-chip and intra-chip optical interconnects," Laser Photonics Rev. **4**(6), 751–779 (2010).
129. B. Song, C. Stagarescu, S. Ristic, A. Behfar, and J. Klamkin, "3D integrated hybrid silicon laser," Opt. Express **24**(10), 10435–10444 (2016).
130. M. Lamponi, S. Keyvaninia, C. Jany, F. Poingt, F. Lelarge, G. de Valicourt, G. Roelkens, D. Van Thourhout, S. Messaoudene, J.-M. Fedeli, and G. H. Duan, "Low-threshold heterogeneously integrated InP/SOI lasers with a double adiabatic taper coupler," IEEE Photon. Technol. Lett. **24**(1), 76–78 (2012).
131. R. Loi, J. O'Callaghan, B. Roycroft, C. Robert, A. Fecioru, A. J. Trindade, A. Gocalinska, E. Pelucchi, C. A. Bower, and B. Corbett, "Transfer printing of AlGaInAs/InP etched facet lasers to Si substrates," IEEE Photonics J. **8**(6), 1–10 (2016).
132. J. Zhang, B. Haq, J. O'Callaghan, A. Gocalinska, E. Pelucchi, A. J. Trindade, B. Corbett, G. Morthier, and G. Roelkens, "Transfer-printing-based integration of a III-V-on-silicon distributed feedback laser," Opt. Express **26**(7), 8821–8830 (2018).

Optical Materials EXPRESS

133. A. De Groote, P. Cardile, A. Z. Subramanian, A. M. Fecioru, C. A. Bower, D. Delbeke, R. Baets, and G. Roelkens, "Transfer-printing-based integration of single-mode waveguide-coupled III-V-on-silicon broadband light emitters," Opt. Express **24**(13), 13754–13762 (2016).
134. L. Liu, R. Loi, B. Roycroft, J. O'Callaghan, A. J. Trindade, S. Kelleher, A. Gocalinska, K. Thomas, E. Pelucchi, C. A. Bower, and B. Corbett, "Low-power-consumption optical interconnect on silicon by transfer-printing for used in opto-isolators," J. Phys. D: Appl. Phys. **52**(6), 064001 (2019).